Modeling and Optimization of Permanent Magnet Motors

by

Andrew P. Pinkham

Submitted to the Department of Electrical Engineering and Computer Science

in Partial Fulfillment of the Requirements for the Degree of

Master of Engineering in Electrical Engineering and Computer Science

at the Massachusetts Institute of Technology

August 2008

Author_____

Department of Electrical Engineering and Computer Science
August 22, 2008

Certified by_____

Elliot Ranger
Group Leader, Charles Stark Draper Laboratory
VI-A Company Thesis Supervisor

Certified by_____

James L. Kirtley Jr.
Professor of Electrical Engineering
M.I.T. Thesis Supervisor

Accepted by_____

Arthur C. Smith
Professor of Electrical Engineering
Chairman, Department Committee on Graduate Theses

Modeling and Optimization of Permanent Magnet Motors
by
Andrew P. Pinkham

Submitted to the
Department of Electrical Engineering and Computer Science

August 2008

In Partial Fulfillment of the Requirements for the Degree of
Master of Engineering in Electrical Engineering and Computer Science

ABSTRACT

This thesis develops analytic models for the prediction and optimization of radial-flux permanent magnet motor torque and efficiency. It also facilitates the design optimization of electromagnetically-powered rotorcraft by characterizing optimal motor performance over a wide range of motor mass. The solution of the Poisson Equation, found as a function of the three spatial coordinates, is applied to the prediction of motor fluxes. Back EMF waveforms of prototype motors are measured in order to validate the analytical predictions. The solution of the magneto-quasi-static Maxwell's Equations are applied to the analysis of eddy currents and torque measurements are made to verify the theoretical predictions. Simplified motor models are discovered which yield symbolic solutions for optimal motor parameters as a function of mass. The Monte Carlo method is applied to the empirically-based motor model to compute optimal motor dimensions, number of magnet poles, and magnet height versus motor active mass for arbitrary material parameter values.

Thesis Supervisor: Elliot Ranger
Title: Mixed-Signal Group Leader

Thesis Advisor: Professor James Kirtley
Title: Professor of Electrical Engineering

ACKNOWLEDGEMENTS

August 22, 2008

This thesis was prepared at The Charles Stark Draper Laboratory, Inc., under Draper contract CON01665-1, and under Phase I Nano Air Vehicle contract W31P4Q-06-C-0304, sponsored by DARPA.

Publication of this thesis does not constitute approval by Draper or the sponsoring agency of the findings or conclusions contained herein. It is published for the exchange and stimulation of ideas.

I wish to express my sincere gratitude to my supervisor at Draper Labs, Elliot Ranger, for making it possible for me to write this thesis. Ever since posing the initial design problem to me, he has provided feedback on my progress and has let me pursue my own approach toward solving the problem.

I especially want to thank my MIT thesis supervisor Professor Kirtley for encouraging me to check my answers by thinking about problems in different ways, and to limit the scope of the thesis document. His teaching has greatly increased my fearlessness toward solving hard problems. This thesis has benefited greatly from the corrections and changes suggested by him.

I also want to thank Professor Zahn for teaching me how to solve the fundamental problems which form the core of this thesis, and for writing a very useful reference book. His teaching inspired my interest in pursuing a thesis on this topic.

I want to especially thank Don Fyler of Draper Labs for his important contributions to this thesis. He is a wealth of both practical and theoretical knowledge, and has given me instant and convincing explanations as to whether I should pursue analyses on many different topics and ideas. My sincere thanks go to Don for measuring the back EMFs of the prototype motor structures, and for teaching me about motor fabrication.

I also want to thank Bob Vissar and Steve Bellio for familiarizing me with measurement equipment. I want to thank Steve in particular for advising me about measuring torque accurately with the air-bearing dynamometer. I also thank Sean George for telling me the big picture about propeller efficiency.

My parents have given me lots of love and support, and without them this thesis would not have been possible. I want to thank them for the value they place on education and for supporting me through 19 years of school. To my brother Michael, I want to say thanks for being an inspiring person for me.

Andrew P. Pinkham

Contents

List of Figures

List of Tables

Chapter 1

Introduction

Electric propulsion systems for propeller aircraft have been fostered by recent advancements in permanent magnet motor and energy storage technologies. Small, quiet, high-performance aerial vehicles are now viable and are in demand to perform varied reconnaissance operations spanning a range of flight duration, speed, and vehicle mass requirements. Aerial vehicle propulsion systems are optimized using brushless motors of various sizes depending on the required total vehicle mass and mission duration.

1.1 Thesis Objective and Overview

This thesis endeavors to characterize optimal motor designs so that aerial vehicle motor and battery masses can be quickly and accurately optimized. The class of machines known as permanent magnet (PM) brushless DC motors are investigated for aerial vehicle propulsion because they offer high efficiency, torque density, and reliability and because they lend themselves to being easily constructed. High-strength magnets on the rotor induce most of the voltage at the armature terminals, enabling high efficiency and torque density. PM motors are synchronous because the mechanical and electrical frequencies have a constant relationship. Brushless DC control is an

electronic control technique which makes the synchronous machine behave like a brushed DC commutator machine. This control technique is employed because the propeller must be able to rapidly accelerate from standstill.

This thesis first develops a model for estimating the parameters and losses in PM motors. The model is then refined so that its predictions correspond well with empirical measurements. The motor design parameters, such as the number of permanent magnets, are then optimized under the assumption that these variables are unconstrained. Analytic expressions for these parameters are given as functions of motor mass and material properties. The motor attribute that is optimized is torque for given efficiency and speed. The optimal efficiency for given torque and speed is then provided so that the optimal battery mass for given total vehicle mass and propeller torque and speed can be estimated.

1.2 Permanent Magnet Motor Operation

Motors are designed to convert electric power–voltage times current at the electrical terminals–to mechanical power–torque times speed of the motor shaft. As shown in Fig. 1.1, the rotor of the machine is designed to produce spatially varying flux-density. The rotor frame is defined by direct and quadrature axes where the quadrature axis leads the direct axis by 90 degrees and the direct axis is chosen to align with the highest flux-density. Voltages induced in stator conductors by the airgap flux-density interact with currents in these conductors to yield power. The stator currents and voltages are projected onto the rotating d-q frame to produce the resultant quantities i_d, i_q, etc.

If the stator currents are driven by a single-phase source, then i_d and i_q are not constant. For example, when the q-axis lies between stator coils i_q is zero and therefore the electromagnetic torque is zero independently of the current. The fluctuation of i_d decreases efficiency and also produces load torque ripple which may have undesirable effects.

By using multiple phases the above problems may be mitigated since it is possible to obtain

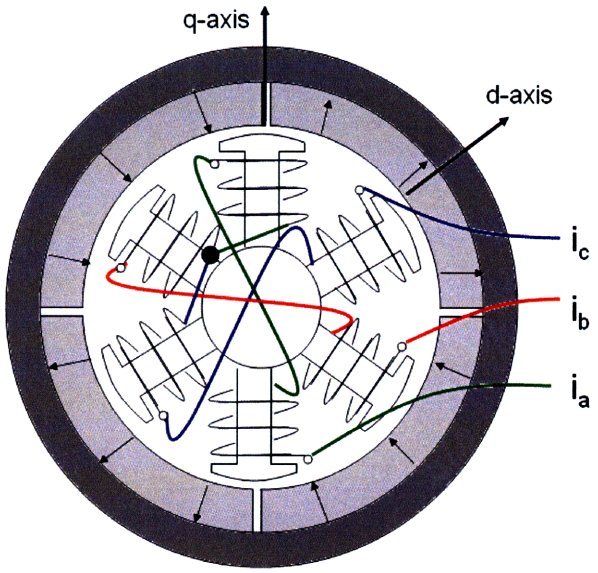

Figure 1.1: Example of a three-phase permanent magnet motor

d-q frame currents which are independent of position. In Appendix A it is shown that if the d and q axis inductances are equal, as they are in Fig. 1.1, then the net torque due to the interaction between i_d and i_q and the fluxes produced by these currents is zero. Therefore, the most torque for a given current magnitude is produced by controlling i_d to be zero. As derived in Appendix A, balanced stator currents produce constant d-q currents. The calculation of electromagnetic output torque only requires solving for the permanent magnet field distribution in the winding region. This problem is addressed in Chapter 2.

1.3 Related Works

The motor shown in Fig. 1.1 works by the interaction between radially-directed flux and axially-directed current. If the motor layout is instead as shown in Fig. 1.2(b), axially-directed flux and radially-directed current can be employed to produce torque. The design study in [7] shows that radial-flux and axial-flux structures have similar efficiency and torque density, and other published studies have reached similar conclusions. Fabrication of the laminated, slotted stator, which is

the structure found to yield the best motor performance, is more well-known to the author for the radial-flux structure than it is for the axial-flux structure. Therefore, exclusively radial-flux structures are optimized and built in this thesis.

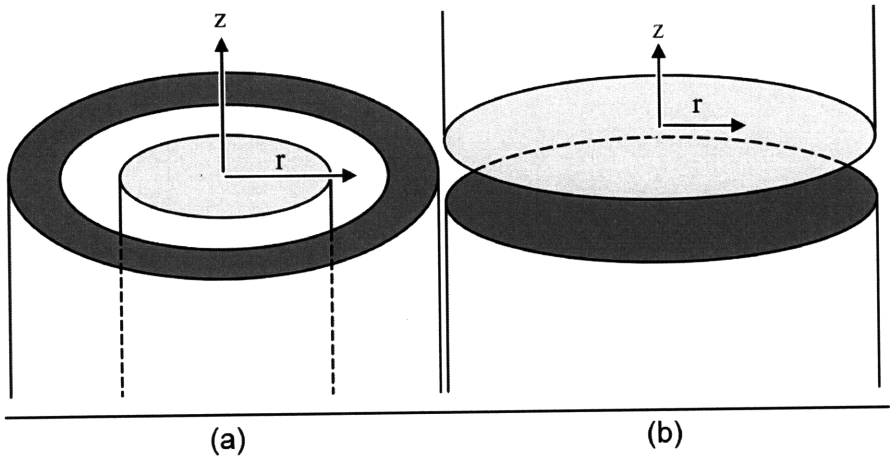

Figure 1.2: (a) Radial-flux geometry, (b) axial-flux geometry

The permanent magnets on the rotor can be configured in various ways to yield the desired motor performance. Of the various possible rotor topologies, the structure shown in Fig. 1.1 with radially magnetized permanent magnets attached to the rotor surface is deemed optimal for this application. Several studies have proven helpful in reaching this conclusion. As shown in [10, p. 23], for a fixed mass of magnet material surface-mount magnets produce more airgap flux than embedded magnets produce. This is because a given surface-mount magnet mass has less end flux leakage than would the same mass of embedded magnet material. On the other hand, an embedded magnet rotor may be designed to produce saliency torque. A complete analysis to determine the maximum torque density under each rotor topology is beyond the scope of this thesis. However, the salient rotor's iron mass must be larger than that of the surface-mount rotor which produces the same airgap flux in a motor with a uniform airgap thickness. It is likely that the higher rotor mass outweighs the torque increase and results in a lower torque density.

Another rotor design uses a Halbach array to augment the magnetic field on the airgap side of the rotor by using permanent magnets with alternating radial and azimuthal magnetization. An ex-

terior rotor machine using a Hallbach array has been examined in [6, p. 49]. This study proves that for a fixed magnet mass the Halbach array yields higher torque only if there is no ferromagnetic backing or if the magnets are sufficiently thick to make the ferromagnetic backing negligible. In these cases the Halbach array produces higher torque because the flux is augmented on one side of the array. In this thesis, rotor backiron provides the mechanical structure as well as the magnetic return and it cannot be replaced by a non-ferromagnetic material that is substantially lighter yet equally as strong as steel. Backiron is therefore required, in which case radially magnetized magnets produce higher torque than a Halbach array for the same magnet mass. This is because backiron makes the azimuthally magnetized magnets relatively less useful compared to the radially magnetized magnets.

Chapter 2

Permanent Magnet Field Analysis

In this chapter the magnetic field solution of a radial-flux permanent magnet machine is computed as a function of all three coordinates. As shown in Fig. 2.1, the motor model is solved using cylindrical co-ordinates. A single co-ordinate system is fixed to the rotor and stator and therefore there are no fluctuating fields.

2.1 Three-Dimensional Field Solution

Because there are no time-varying fields, there is no electric field and Maxwell's equations simplify so that the magnetic field is just the negative gradient of a scalar potential ψ:

$$\vec{H} = -\nabla\psi \tag{2.1}$$

In the permanent magnet region the equation $\vec{B} = \mu_0(\mu_R\vec{H} + \vec{M})$ holds, where μ_R is given in Chapter 4 and is assumed to be isotropic. The divergence of Eq. (2.1) is:

$$\nabla^2\psi = -\nabla\cdot\vec{H} = \frac{1}{\mu_R}\nabla\cdot\vec{M} \tag{2.2}$$

The magnetization $\vec{M}$ is entirely radially directed and is assumed to be constant throughout the magnet volume. We define $M(\theta, z) \equiv \frac{1}{\mu_R}\vec{M} \cdot \hat{r}$ so that the above equation simplifies to:

$$\frac{1}{r}\frac{\partial}{\partial r}\left(r\frac{\partial \psi}{\partial r}\right) + \frac{1}{r^2}\frac{\partial^2 \psi}{\partial \theta^2} + \frac{\partial^2 \psi}{\partial z^2} = \frac{1}{r}M(\theta, z) \tag{2.3}$$

To solve this equation we try a separable solution $\psi = R(r)\cos(p\theta)\cos(kz)$ since this form is known to be the only solution to the homogeneous Laplace equation. If we also try sinusoidally distributed magnetization $M(\theta, z) = M\cos(p\theta)\cos(kz)$ we obtain:

$$\left(r^2\frac{d^2R}{dr^2} + r\frac{dR}{dr} - (k^2r^2 + p^2)R\right)\cos(p\theta)\cos(kz) = rM\cos(p\theta)\cos(kz) \tag{2.4}$$

We see that the sinusoidal θ and z dependencies cancel and this therefore yields an ODE for R(r). If we then perform the change of variable $x = jkr$ we obtain:

$$x^2\frac{d^2R}{dx^2} + x\frac{dR}{dx} + (x^2 - p^2)R = -\frac{jx}{k}M \tag{2.5}$$

which is just the inhomogeneous Bessel differential equation. The most general solution for $R(r)$ is a particular solution $R_p(r)$ plus the general homogeneous solution $R_h(r)$. A real-valued homogeneous solution is given by: [11, p. 282]

$$\begin{aligned} R_h(r) &= Aj^{-p}J_p(jkr) + B\frac{\pi}{2}j^{p+1}[J_p(jkr) + jY_p(jkr)] \\ &= AI_p(kr) + BK_p(kr) \end{aligned} \tag{2.6}$$

where $I_p(kr)$ and $K_p(kr)$ are the modified Bessel functions and A and B are arbitrary constants. In the limit $k \rightarrow 0$ this problem becomes two-dimensional and the modified Bessel functions approach $r^{\pm p}$.

A particular solution to Eq. (2.4) is found using a numerical technique. After writing this

second-order ODE as two first-order ODEs, the Runge-Kutta method in Matlab is used to solve

$$\begin{aligned}\frac{dR_p}{dr} &= \dot{R} \\ \frac{d\dot{R}}{dr} &= -\frac{1}{r}\dot{R} + (k^2 + \frac{p^2}{r^2})R + \frac{M}{r}\end{aligned}$$

In the limit $k \to 0$ and for small r so r^2 is neglected, the problem becomes two-dimensional and a particular solution to Eq. (2.4) is $R_p(r) = \frac{rM}{1-p^2}$.

The magnetic field solution is:

$$\begin{aligned}\vec{H} &= -\nabla(R_h(r) + R_p(r))\cos(\theta)\cos(z) \\ &= -\frac{d}{dr}(AI_p(kr) + BK_p(kr) + R_p(r))\cos(p\theta)\cos(kz)\hat{r} \\ &\quad +\frac{p}{r}(AI_p(kr) + BK_p(kr) + R_p(r))\sin(p\theta)\cos(kz)\hat{\theta} \\ &\quad +k(AI_p(kr) + BK_p(kr) + R_p(r))\cos(p\theta)\sin(kz)\hat{z}\end{aligned} \tag{2.7}$$

The sinusoidal form of magnetization which solved the Poisson equation also allows for the magnetization to be written as a Fourier series. The permanent magnets are assumed to produce a square wave of magnetization in θ and z. This has the 2-D Fourier series representation:

$$M(\theta, z) = \sum_{m,odd}\sum_{n,odd} M_n \cos(mp\theta)^\top \cos(nkz) \tag{2.8}$$

where p, the number of pole pairs, and k are the fundamental wavenumbers, and

$$M_n = M\frac{16}{\pi^2 mn}\sin\left(m\frac{\theta_m}{2}\right)\sin\left(n\frac{\theta_z}{2}\right) \tag{2.9}$$

where θ_m is the pole arc in *electrical* measure, and θ_z is given by Eq. (2.10) in order to model the stator core length as being shorter than the fundamental wavelength. By making θ_z much less than

π we can effectively model a single motor. Moreover, it is possible to relate the value of θ_z to the physical parameters. Notice from Eq. (2.7) that where the fundamental in the z dimension is zero, H_r and H_θ are zero and the field is entirely z directed. By using a Fourier series we thus have the equivalent of ferromagnetic boundaries at the ends of the motor. This analysis is thereby capable of modeling an enclosed outrunner motor for which the rotor structure forms the ferromagnetic boundaries. To make the boundaries a distance g_z from the ends of the magnets, as shown in Fig. 2.1, θ_z is given by

$$\theta_z = \frac{\pi}{1 + 2g_z/L_m} \tag{2.10}$$

2.2 Motor Model

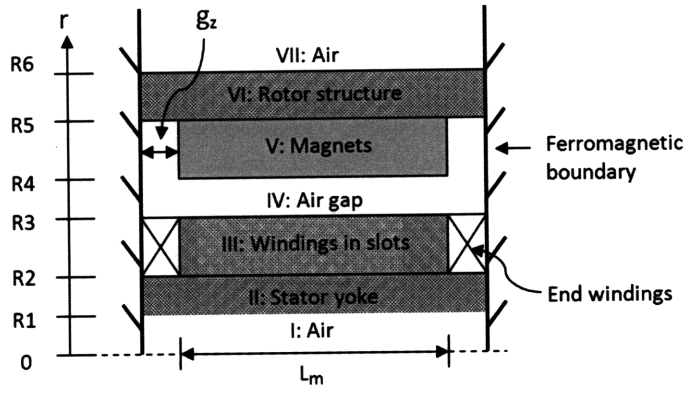

Figure 2.1: Radial-flux cylindrically-symmetric motor model

The motor model consists of the seven regions shown in Fig. 2.1. There are no constant θ boundaries so there are two arbitrary constants in each region. Maxwell's equations give boundary conditions at each interface. The tangential H field is continuous if both H_θ and H_z are continuous. From Eq. (2.7) we see that a single equation satisfies the boundary condition on both of these components. The continuity of B_r yields the second equation at each interface. We also immediately know that B_1 and A_7 are zero because the potential must be finite everywhere. At each of the boundaries between regions the relationship $B_{rx} = \mu_0(\mu_x H_{rx} + M_n)$ and Eq. (2.7) yield two

equations. The 12 equations in 12 unknowns are written as a matrix equation:

$$\begin{bmatrix}
\mu_1 dI_1 & -\mu_2 dI_1 & -\mu_2 dK_1 & 0 & 0 & 0 & 0 & 0 & 0 & 0 & 0 & 0 \\
0 & \mu_2 dI_2 & \mu_2 dK_2 & -\mu_3 dI_2 & -\mu_3 dK_2 & 0 & 0 & 0 & 0 & 0 & 0 & 0 \\
0 & 0 & 0 & \mu_3 dI_3 & \mu_3 dK_3 & -\mu_4 dI_3 & -\mu_4 dK_3 & 0 & 0 & 0 & 0 & 0 \\
0 & 0 & 0 & 0 & 0 & \mu_4 dI_4 & \mu_4 dK_4 & -\mu_5 dI_4 & -\mu_5 dK_4 & 0 & 0 & 0 \\
0 & 0 & 0 & 0 & 0 & 0 & 0 & \mu_5 dI_5 & \mu_5 dK_5 & -\mu_6 dI_5 & -\mu_6 dK_5 & 0 \\
0 & 0 & 0 & 0 & 0 & 0 & 0 & 0 & 0 & \mu_6 dI_6 & \mu_6 dK_6 & -\mu_7 dK_6 \\
I_1 & I_1 & -K_1 & 0 & 0 & 0 & 0 & 0 & 0 & 0 & 0 & 0 \\
0 & I_2 & K_2 & -I_2 & -K_2 & 0 & 0 & 0 & 0 & 0 & 0 & 0 \\
0 & 0 & 0 & I_3 & K_3 & -I_3 & -K_3 & 0 & 0 & 0 & 0 & 0 \\
0 & 0 & 0 & 0 & 0 & I_4 & K_4 & -I_4 & -K_4 & 0 & 0 & 0 \\
0 & 0 & 0 & 0 & 0 & 0 & 0 & I_5 & K_5 & -I_5 & -K_5 & 0 \\
0 & 0 & 0 & 0 & 0 & 0 & 0 & 0 & 0 & I_6 & K_6 & -K_6
\end{bmatrix}$$

$$\times \begin{bmatrix} A_1 \\ A_2 \\ B_2 \\ A_3 \\ B_3 \\ A_4 \\ B_4 \\ A_5 \\ B_5 \\ A_6 \\ B_6 \\ B_7 \end{bmatrix} = \begin{bmatrix} 0 \\ 0 \\ 0 \\ -\mu_0 M_n + \mu_5 \frac{d}{dr} R_p(R_4) \\ \mu_0 M_n - \mu_5 \frac{d}{dr} R_p(R_5) \\ 0 \\ 0 \\ 0 \\ 0 \\ R_p(R_4) \\ -R_p(R_5) \\ 0 \end{bmatrix}$$

where

$$dI_x \equiv \frac{d}{dr} I_p(kr)|_{R_x} = \frac{p}{R_x} I_p(kR_x) - kI_{p+1}(kR_x) \tag{2.11}$$

Given numeric parameter values, the Matlab functions in Section B.1 solve this equation numerically for each magnetization harmonic and sum the field distributions in θ and z from each harmonic.

2.2.1 Saturation

The permeability μ_x used above for $x = 1, 2, 3...7$ is the ratio $\frac{|B_x|}{|H_x|}$. Since the azimuthal flux-density in the rotor backiron and the radial flux density in the stator teeth are nearly uniform, each

region may be accurately described by a constant permeability. For the magnetic field solution to be valid, the points given by H and μH in the iron regions must lie on the empirically determined hysteresis curve of the lamination material. The 3D fieldsolver in Section B.1 is itself a nonlinear function whose inputs are the μ values and whose outputs are the H values. In each region this function equals the nonlinear function $H(\mu)$ derived from the hysteresis curve. The Matlab functions in Section B.1 simultaneously solve the two multivariable nonlinear equations for the relative permeabilities and magnetic field amplitudes.

2.3 Results and Finite Element Comparison

2.3.1 Airgap Field Distributions

Fig. 2.2 and Fig. 2.3 show the radial mid-gap flux-density solved using the analytical method presented in this chapter, and solved using Ansoft Maxwell 3D. The parameters $p = 2$, $g_z = 0$, $B_r = 1.4T$, $R_1 = 2mm$, $R_3 = 5mm$, and $h_m = 1mm$ were used. To plot the finite element data, the numerical values of the flux density component normal to the stator surface at various points were written to a file. These data points were clustered into 120 by 60 cells in θ and z and the average of the points in each cell was taken as the normal flux density of the cell.

Fig. 2.4 shows the mid-gap radial flux-density for various values of the end-gap g_z. Recall that ferromagnetic boundaries, at which the radial flux-density is zero and is entirely axially directed, are located distances g_z from the ends of the iron stator core. The iron core extends from $z = -.5[mm]$ to $z = .5[mm]$, and the values of g_z are shown in the legend. When the gap is small, much of the permanent magnet flux is shorted-out through the end-bell. The field amplitude is smallest when the end-gap is small, and the field calculation confirms this intuition. The "tails" of the distribution extend until the ferromagnetic boundaries, but the field decays quickly at the ends of the stator core. The radial flux-density is a maximum when the end-bell boundaries are

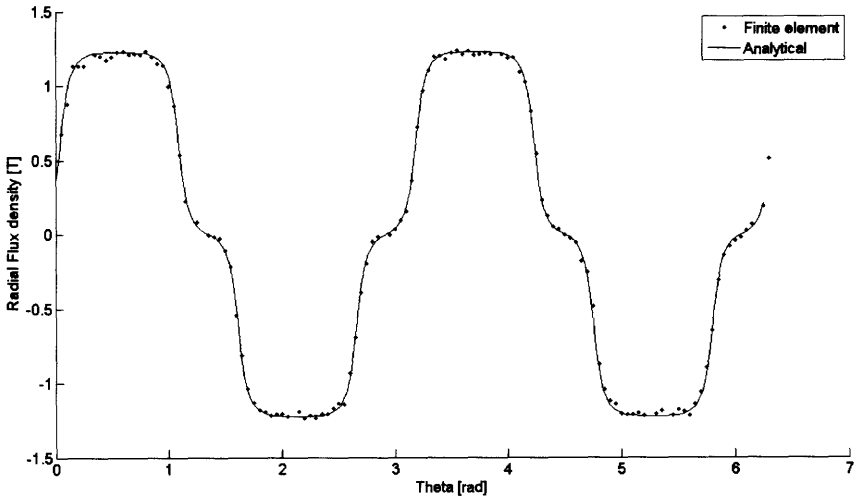

Figure 2.2: Radial Field as Function of θ

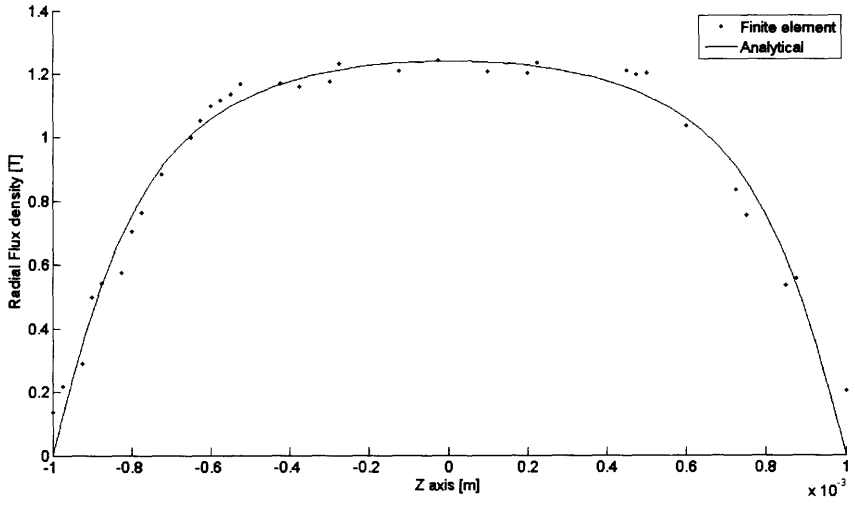

Figure 2.3: Radial Field as Function of z

infinitely far away. However, as long as the end-gap is at least equal to the stator axial length, the radial flux-density is approximately at its maximum.

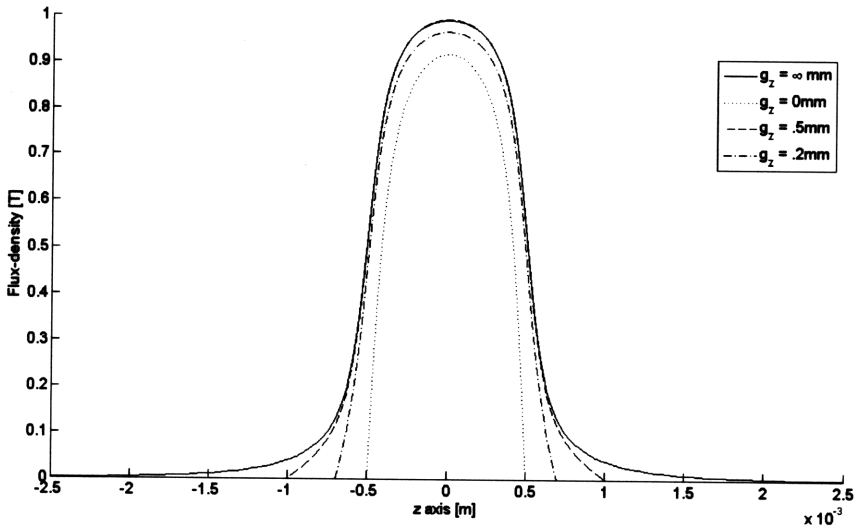

Figure 2.4: Radial flux-density vs. z for several values of the end-gap g_z between the stator core and end-bell. The stator core is $1[mm]$ in length and the end-gap values are shown in the legend.

2.3.2 2-D Vector Fields

The magnetic field is computed at points evenly spaced in three dimensions, as opposed to along lines of constant field magnitude. It is therefore easiest to draw separate arrows at each point than it is to calcuate magnetic field lines, although this is perhaps a less intuitive way of visualizing the two-dimensional magnetic field.

Fig. 2.5 shows a flattened view of the mid-gap magnetic field as a function of θ and z for a two-pole rotor, and therefore only the $\hat{\theta}$ and $\hat{z}$ field components are shown. The relative motion gap here is .2mm. This plot is provided to show the flux path between the magnets and the rotor end bell, and the flux path between magnets.

Fig. 2.6 shows the vector field at $z = 0$ in the magnet region and in the airgap. As before, the outlines of the magnets are shown. The purpose of this plot is to show the field lines in the airgap

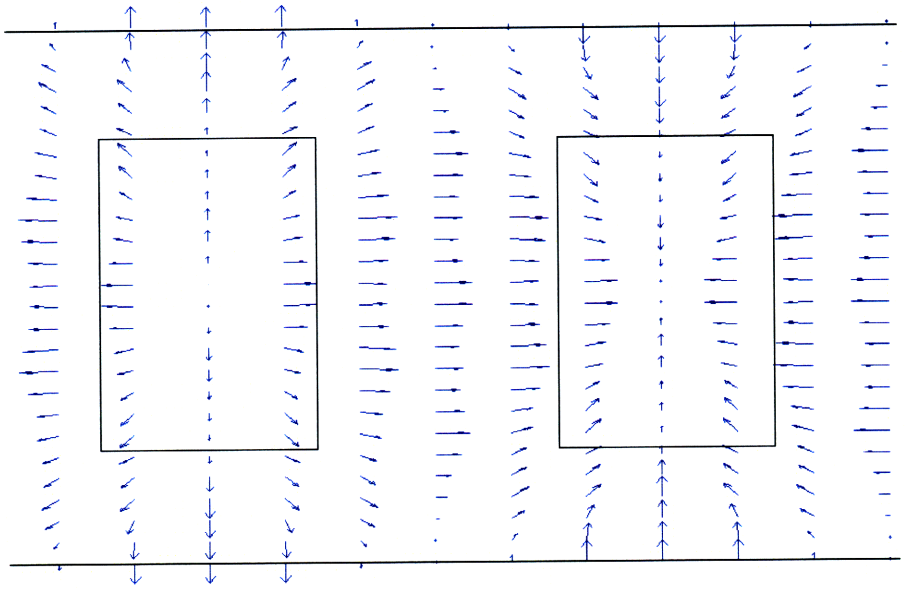

Figure 2.5: Vector field in z (vertical) and θ (horizontal). The dimensions and polearc of the magnets are given by the two rectangles. The horizontal black lines are at the locations of the ferromagnetic axial boundaries. The magnet surface is .1mm radially above the surface whose magnetic field is shown here

region as well as to illustrate the flux paths which exist in both the magnet and airgap regions.

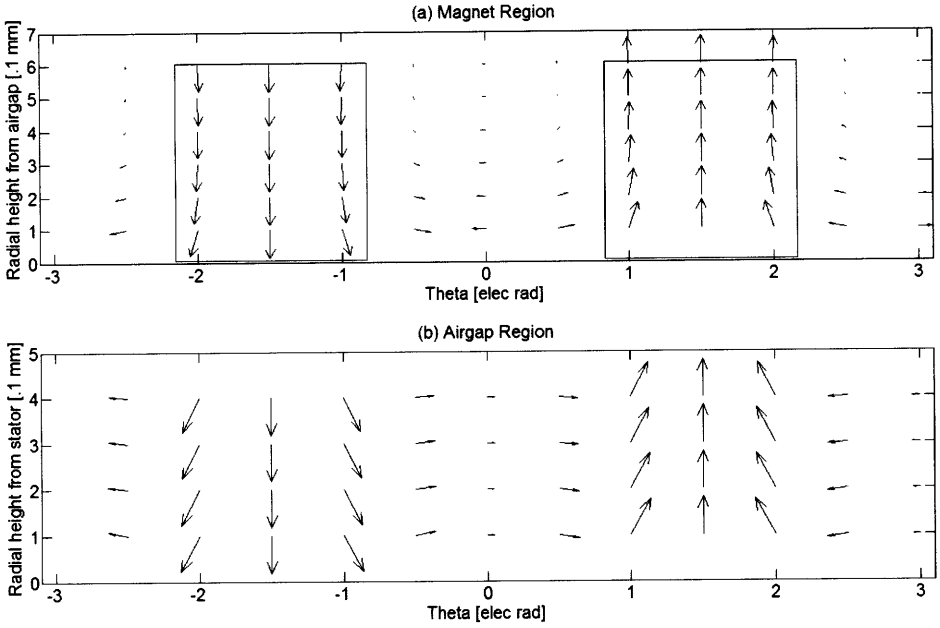

Figure 2.6: Vector field in the magnet region (above) and airgap region (below)

Chapter 3

Eddy Current Analysis

In this chapter a model for the prediction of eddy current core loss is developed. An analytical eddy current model is developed for the radial-flux structure using polar coordinates. Eddy-current core loss is a result of the rotating magnetic fields in the stator core and the conductivity of the core material.

The analysis is performed in the magneto-quasistatic limit since the physical dimensions of the structure are very small compared to the wavelength of the electromagnetic waves which it radiates. In this limit the equation for current density given by Maxwell's Equations is:

$$\nabla^2 \vec{J} = \mu\sigma \frac{\partial \vec{J}}{\partial t} \tag{3.1}$$

The solution for the current distribution given by this equation already accounts for the forces acting internally between the individual current elements, since electromagnetic forces are not a separate phenomenon from Maxwell's Equations.

3.1 Current and Field Solutions

The current density is induced by a rotating wave of radial magnetization of infinite axial length. The current density is therefore of the form:

$$J_n = Re\left(\underline{J}_n(r)e^{jn(\omega t - p\theta)}\right)\hat{z} \tag{3.2}$$

where $\underline{J}_n(r)$ is complex. Since J is entirely z-directed the vector Laplacian simplifies to the scalar Laplacian, and therefore Eq. (3.1) simplifies to the scalar Poisson equation. Substitution of the current density into Eq. (3.1) yields

$$r^2\frac{d^2\underline{J}_n}{dr^2} + r\frac{d\underline{J}_n}{dr} - (jn\omega\mu\sigma r^2 + (np)^2)\underline{J}_n = 0 \tag{3.3}$$

By using the change of variable $x = jr\sqrt{jn\omega\mu\sigma} = \frac{(1-j)}{\delta}r$, where the skin depth is $\delta = \sqrt{2/(n\omega\mu\sigma)}$, we obtain

$$x^2\frac{d^2\underline{J}_n}{dx^2} + x\frac{d\underline{J}_n}{dx} + (x^2 - (np)^2)\underline{J}_n = 0 \tag{3.4}$$

which is the bessel differential equation. A general solution to this special case of Eq. (3.1) is:

$$\underline{J}_n(r) = A_n J_{np}\left(\frac{(1-j)}{\delta}r\right) + B_n Y_{np}\left(\frac{(1-j)}{\delta}r\right) \tag{3.5}$$

where A and B are complex constants. The magnetic field is found using Faraday's Law

$$\vec{H}_n = Re\left(-\frac{1}{jn\omega\mu\sigma}\nabla\times\vec{J}\right) = Re\left(-\frac{1}{jn\omega\mu\sigma}\left(\frac{jnp}{r}\underline{J}_n(r)\hat{r} - \frac{d}{dr}\underline{J}_n(r)\hat{\theta}\right)e^{jn(\omega t - p\theta)}\right) \tag{3.6}$$

The flux-linkage per unit length of the r-z plane located at $\theta = \omega t/p$ is given by $\mu_0\int_0^R H_\theta dr$, which is simply equal to $Re\left(\frac{1}{jn\omega\mu\sigma}\underline{J}_n(R)\right)$.

3.1.1 Motor Model

The rotating wave of radial magnetization is modeled as a rotating step-wave which has the Fourier series representation:

$$\vec{M} = Re\left(\sum_{n,odd} M_n e^{jn(\omega t - p\theta)}\right)\hat{r} \tag{3.7}$$

where

$$M_n = \frac{4}{n\pi}\sin\left(n\frac{\theta_m}{2}\right)\frac{B_{re}}{\mu_0} \tag{3.8}$$

where θ_m is the magnet polearc and B_{re} is the magnet remenant flux density. The exterior-rotor motor topology is modeled. The magnet array has inner radius R_i and outer radius R_o and is backed by a ferromagnetic boundary. The stator has radius R, bulk conductivity σ, and permeability μ. The arbitrary constants in the three-region Poission equation problem are found by solving

$$\begin{bmatrix} R_o^{np} & R_o^{-np} & 0 & 0 & 0 \\ -\mu_r np R_i^{np-1} & \mu_r np R_i^{-np-1} & \mu_0 np R_i^{np-1} & -\mu_0 np R_i^{-np-1} & 0 \\ -R_i^{np} & -R_i^{-np} & R_i^{np} & R_i^{-np} & 0 \\ 0 & 0 & \mu_0 np R^{np-1} & -\mu_0 np R^{-np-1} & \mu jnp/(\alpha^2 R) J_{np}(\alpha R) \\ 0 & 0 & jnp R^{np-1} & jnp R^{-np-1} & -1/(2\alpha)(J_{np-1}(\alpha R) - J_{np+1}(\alpha R)) \end{bmatrix} \times \begin{bmatrix} A_{1n} \\ B_{1n} \\ A_{2n} \\ B_{2n} \\ An \end{bmatrix}$$

$$= \begin{bmatrix} -R_o M_n/(1-p^2) \\ -\mu_0 M_n + \mu_0 M_n/(1-p^2) \\ M_n R_i/(1-p^2) \\ 0 \\ 0 \end{bmatrix}$$

where $\alpha = \frac{1-j}{\sqrt{2/(n\omega\mu\sigma)}}$, for each traveling-wave harmonic n.

3.1.2 Airgap Field Distribution

The radial flux-density distribution at the stator surface is

$$B_r = Re\left(\sum_{n,odd} \mu_0 np\left(A_{2n}R^{np-1} - B_{2n}R^{-np-1}\right)e^{jn(\omega t - p\theta)}\right) \tag{3.9}$$

The computation of the airgap field distribution is performed by the Matlab function in Sec-

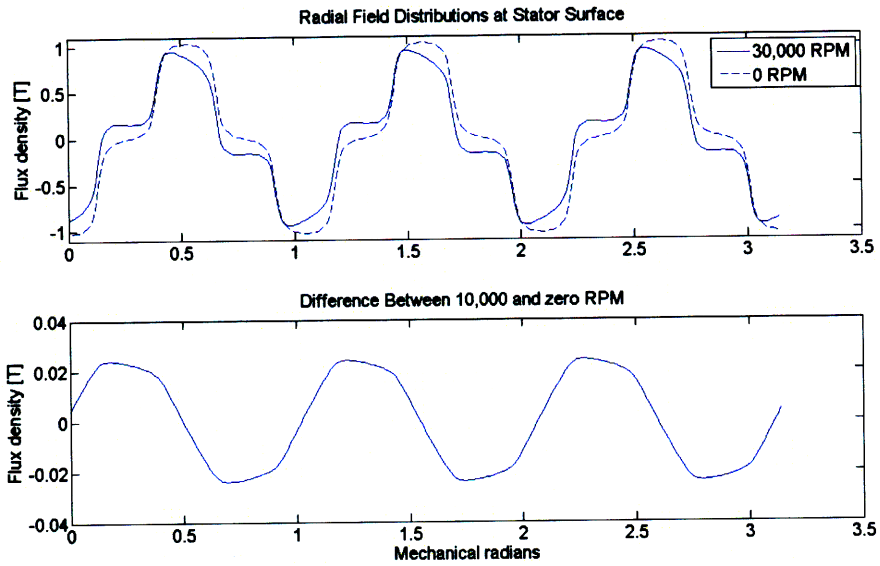

Figure 3.1: Radial flux-densities at stator surface

tion B.3.2. For $\sigma = 5.8 \cdot 10^6$ Siemens/m, $\mu = 1000\mu_0$, $\theta_m = \pi/2$, $B_{rem} = 1.4T$, $p = 4$, $R_o = 6.2mm$, $R_i = 5.2mm$, and $R = 5mm$ the airgap field distributions at zero and 30 kRPM are shown in Fig. 3.1a). The difference between these distributions, which is the field produced by the line-dipole currents at 30 kRPM, is shown in Fig. 3.1b). This accurate field solution based on the MQS model is approximately equal to the static field solution assuming non-fluctuating fields.

The difference between the MQS field solutions and the static field solutions are presented in Fig. 3.2 for four different values of the pole-arc θ_m.

3.1.3 Drag Loss Prediction

Since the rotor has power input only in mechanical form and since all of this power is transferred to the stator, power dissipation due to stator volume currents should be equal to the electromagnetic drag torque between the rotor and stator times their relative speed. The force is calculated in cylindrical coordinates by a volume integral of the Korteweg-Helmholtz force density, which in

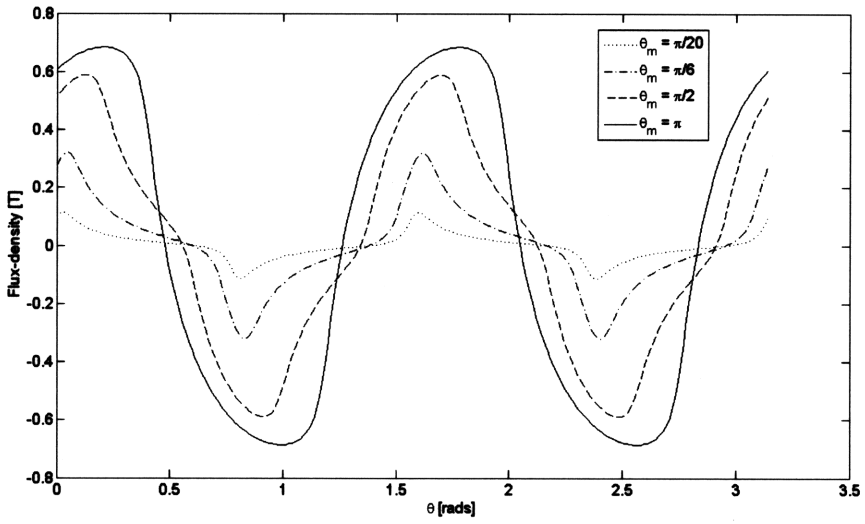

Figure 3.2: Magnetic field distributions produced by induced line-dipole currents

this case simplifies to

$$F = J \times B - \frac{1}{2} H^2 \nabla \mu \tag{3.10}$$

The permeability is a function of radius alone, and therefore the second term in the above expression does not contribute azimuthal force. The time-average azimuthal Lorentz force per unit length is

$$f_{dr} = \frac{1}{2} Re \left(\int_{r=0}^{R} \int_{\theta=0}^{2\pi} J_z B_r r \, dr \, d\theta \right) = \pi Re \left(\int_{r=0}^{R} \underline{J_z} \underline{B_r^*} r \, dr \right) \tag{3.11}$$

The time average power dissipation per unit length is

$$P_{dr} = \int_{r=0}^{R} \int_{\theta=0}^{2\pi} \frac{|J|^2}{\sigma} r \, dr \, d\theta \tag{3.12}$$

The Matlab script in Section B.3.3 computes Eqs. (3.11) and Eq. (3.12) using numerical integration, and then computes $f_{dr} \cdot R$ and P_{dr}/Ω as a function of Ω for $\sigma = 8.4 \cdot 10^6$ Siemens/m, $\mu = 20000\mu_0$. This two curves are shown to be equal. By resorting to numerical integration, it has been demonstrated that the volume force density and ohmic power dissipation methods of calculating drag torque are consistent for any values of permeability and conductivity.

Fig. 3.3 shows drag torque versus speed for four different combinations of permeability and conductivity. The parameters other than the cylinder's σ and μ are the same for all four curves. For $\mu = \mu_0$, drag torque is linear with speed up to 50 kRPM. At higher frequency, the decreasing skin-depth causes drag torque to increase less-than-linear with speed and to eventually decrease with speed. For the same motor but having $\mu = 100\mu_0$, for low speed drag torque increases faster than for the non-permeable cylinder because the flux-density is much higher. High-permeability also implies a smaller skin-depth than for the low-permeability cylinder, however. Therefore, at high enough speed the smaller skin-depth dominates the higher flux-density and the high-permeability cylinder exhibits a lower drag torque than the low-permeability cylinder of the same conductivity and size.

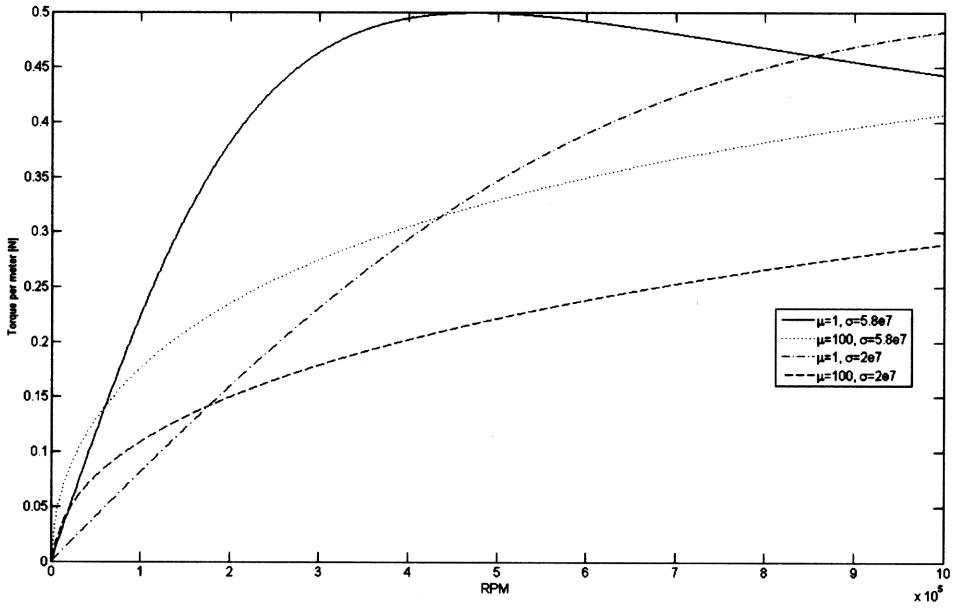

Figure 3.3: Drag torque vs. speed for four different combinations of conductivity and permeability

3.2 Empirical Validation

In this section the analytical model is compared with experimental measurements. The structure which approximates the two-dimensional eddy current problem is shown in Fig. 3.4. It consists of a steel tube, a four-pole permanent magnet array, and a copper cylinder. The permanent magnet axial length of $30mm$ is designed to be much larger than the copper cylinder radius of $1.5mm$ to approximate two-dimensional geometry. The copper cylinder length is longer than the magnets to provide space for eddy currents to flow between the line-dipole currents in the axial region beyond the magnets. To validate the model the drag torque is measured using a precision dynamometer.

As shown in Fig. 3.5, the eddy current structure and drive motor are mounted to plastic stands which are secured to an aluminum rail to keep the shafts aligned. The copper cylinder is connected to a Maxon DC motor through a plastic coupling. An air-bearing provides an ultra-low friction support for the stator so it can move with negligible friction when 40 PSI is supplied to the bearing. An $18mm$ moment arm is attached to the stator which produces force on the load cell when torque is applied to the motor's rotor. A quadrature position encoder attached to the back of the Maxon motor is used to measure speed.

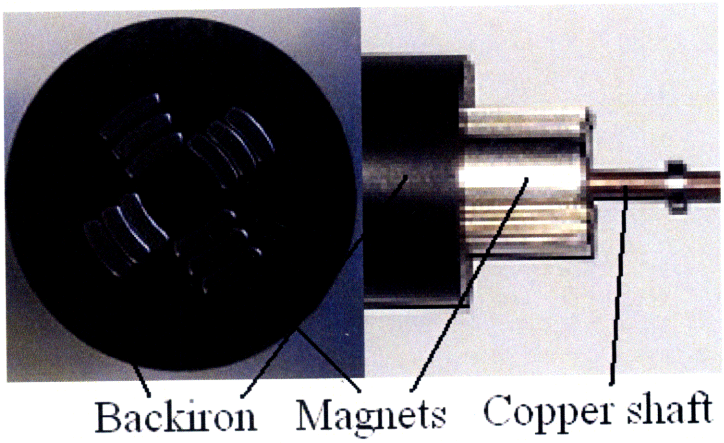

Figure 3.4: 4-pole permanent magnet array

Measurements were taken at speeds between 200 and 18,000 RPM. The magnets were then removed from the tube and torque measurements were taken to measure the bearing drag torque.

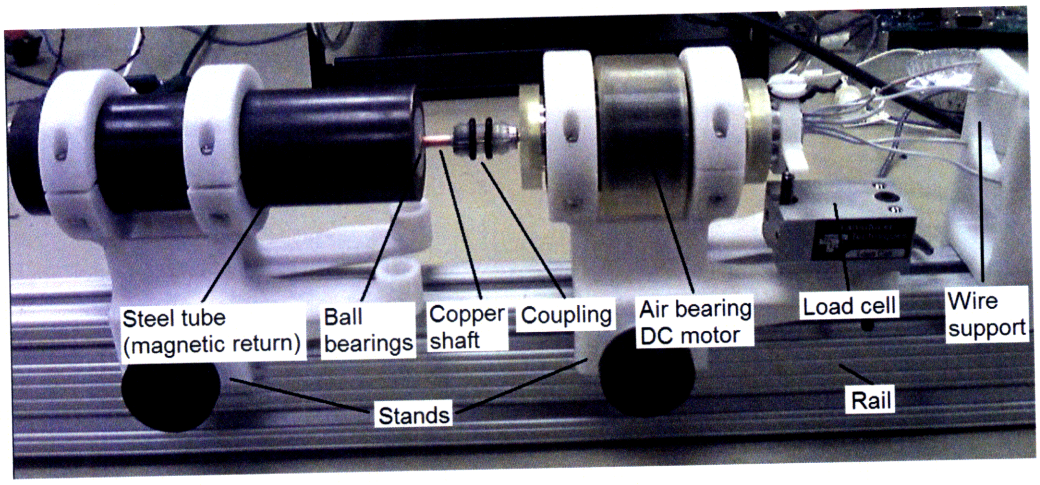

Figure 3.5: Dynamometer setup

The bearing torque was measured to be approximately $.1mN-m$ at 200 RPM and increase linearly to approximately $.14mN - m$ at 18,000 RPM.

As shown in Fig. 3.6, the analytical model predicts that the drag torque is linear with speed up to 18,000 RPM. The measured eddy current drag torque data is in good agreement with the analytical model.

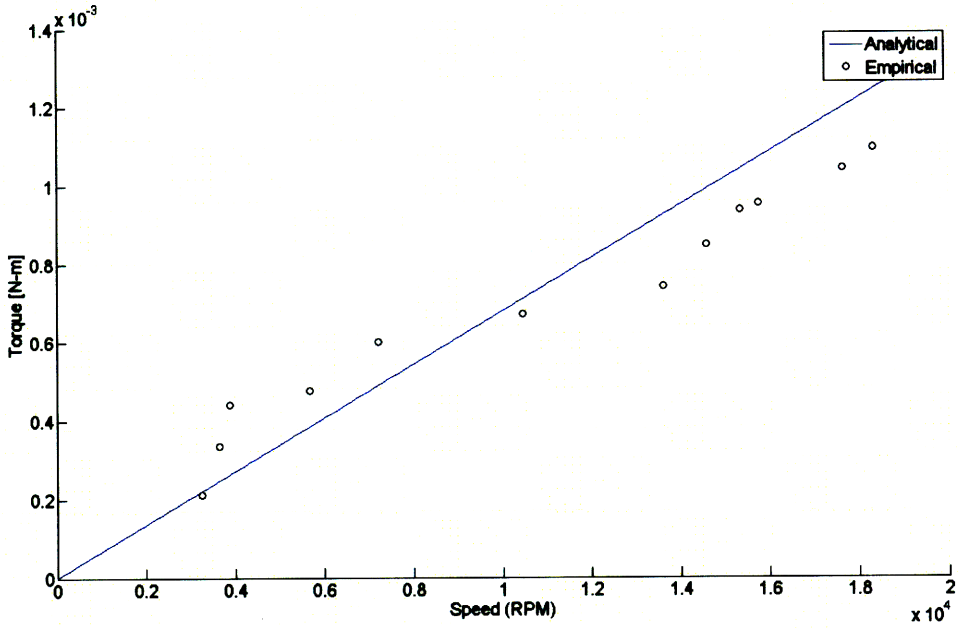

Figure 3.6: Measured eddy current drag torque and analytical prediction

Chapter 4

Hysteresis Analysis

Magnetic hysteresis describes the history-dependent behavior of magnetizable material. In this chapter analysis is performed to develop a model for hysteresis loss in the stator core, and also to characterize the behavior of permanent magnets. The hysteresis loop shown in Fig. 4.1, which is an idealization of the behavior of a ceramic magnetic material, is analyzed in this chapter.

4.1 Magnetic Energy

In this chapter we neglect eddy-currents and fringing fields in the magnetizable material and airgap regions shown in Fig. 4.1. The magnetic fields H_m and H_g are therefore constant in the rectilinear volumes $V_m = Ah$ and $V_g = Ax$ and are entirely x-directed. The magnetic fields in a volume V are capable of performing the differential of electrical work given by $id\lambda$. This is easily seen to be:

$$id\lambda = VHdB \equiv dW_m \tag{4.1}$$

dW_m is defined as the differential of magnetic energy.

In the airgap the flux-density is given by $B_g = \mu_0 H_g$, while in the magnetizable material it is

seen to be:

$$B_m = \mu_0(\mu_R H_m + M(H_m)) \tag{4.2}$$

where μ_R is the relative permeability which is a constant, and where $M(H_m)$ is the magnetization which depends on the magnetic field in the material. $M(H,T)$ is known as the equation of state (EOS) of the magnetizable material where T is the temperature.[9] The EOS is given by the hysteresis loop in Fig. 4.1 for a given constant temperature.

The differential of magnetic energy is given by:

$$dW_m = Ah\mu_0(\mu_R H_m dH_m + H_m dM(H_m)) + Ax\mu_0 H_g dH_g \tag{4.3}$$

We write the two magnetic circuit equations which are dependent on the EOS $M(H_m)$:

$$H_g = \mu_R H_m + M(H_m) \tag{4.4}$$

$$H_m(h + x\mu_R) + xM(H_m) = Ni \tag{4.5}$$

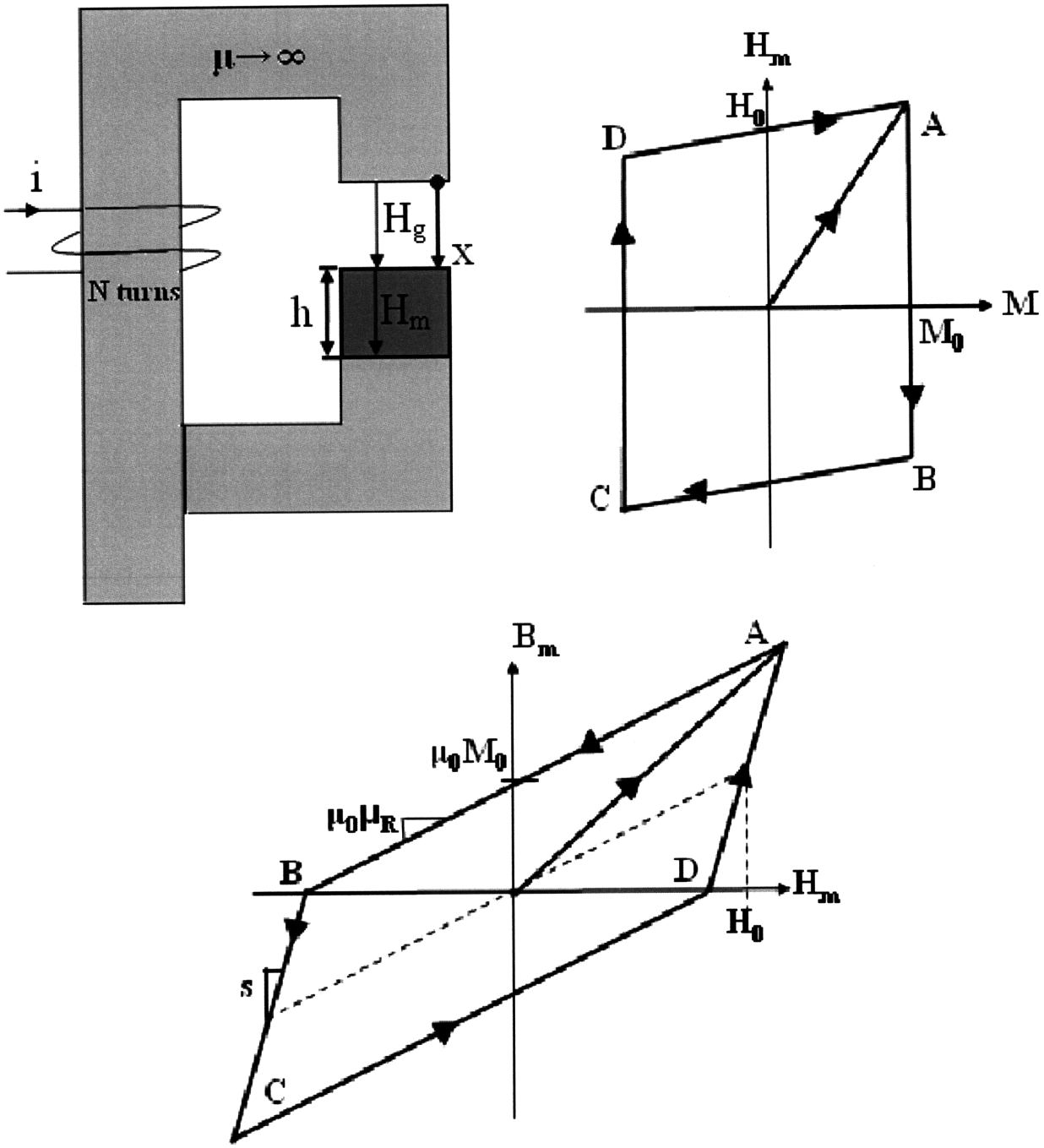

Figure 4.1: Hysteresis loops of the magnetizable material, shown with B_m vs. H_m and H_m vs. M diagrams. The vertices of the hysteresis loop are labeled A,B,C,D. The structure has cross-sectional area A.

4.2 Hysteresis Loop

We first consider magnetizing the material along the path from the origin to the point given by vertex A. As shown in Fig. 4.1 the EOS along this path is approximated as being $M(H_m) = H_m$ and therefore:

$$H_m = \frac{Ni}{h + x(1 + \mu_R)} \tag{4.6}$$

The energy input to the magnetizable material is:

$$\int_o^{B_m} H_m(B_m^{'}) dB_m^{'} = \frac{1}{2} B_m H_m$$

so energy is put into the material. The magnetization work is:

$$\int_o^{M} \mu_0 H_m(M^{'}) dM^{'} = \frac{\mu_0}{2} H_m^2$$

Once the material is magnetized it is idealized as having constant magnetization until the point given by vertex B. As shown in Fig. 4.1, the EOS along the path A→B is $M(H_m) = M_0$ and therefore

$$H_m = \frac{Ni - xM_0}{h + x\mu_R} \tag{4.7}$$

The energy input to the material is:

$$\int_A^{B_m} H_m(B_m^{'}) dB_m^{'} = \frac{B_m}{\mu_R} \left(\frac{B_m}{2\mu_0} - M_0 \right) - \frac{B_A}{\mu_R} \left(\frac{B_A}{2\mu_0} - M_0 \right)$$

where $B_A = \mu_0 \mu_R (H_0 + \frac{M_0}{s}) + \mu_0 M_0$ is the flux-density at vertex A. Over the complete path A→B net energy is removed from the material, since the magnetization work is $\int_A^M \mu_0 H(M^{'}) dM^{'} = 0$ and the absolute value of H_m is smaller at B than at A.

The magnetization is reversed if the field in the material becomes more negative. Along the

path B→C the EOS is given by $M(H_m) = s(H_m + H_0)$ where $s = \frac{dB_m}{dH_m}$ is the slope of the line. Therefore the magnetic field is:

$$H_m = -H_0 + \frac{Ni + H_0(h + x)}{h + x(1 + s)}$$

The energy input to the material is:

$$\int_B^{B_m} H_m(B_m^{'})dB_m^{'} = \frac{1}{2}B_m\left(H_m - \frac{M_0}{\mu_R}\right)$$

so net energy is put into the material. The magnetization work is

$$\int_B^M \mu_0 H_m(M^{'})dM^{'} = \frac{1}{2}(M_0 - M)\left(-H_m + \frac{M_0}{\mu_R}\right)$$

The material then has constant negative magnetization with the EOS $M(H_m) = -M_0$. The energy input to the material is:

$$\int_C^{B_m} H_m(B_m^{'})dB_m^{'} = \frac{B_m}{\mu_R}\left(\frac{B_m}{2\mu_0} + M_0\right) - \frac{-B_A}{\mu_R}\left(\frac{-B_A}{2\mu_0} + M_0\right)$$

so net energy is removed from the material going from C to D, since the magnetization work is $\int_C^M \mu_0 H(M^{'})dM^{'} = 0$ and the absolute value of H_m decreases.

Along the path D→A the EOS is $M(H_m) = s(H_m - H_0)$. Therefore the magnetic field is:

$$H_m = H_0 + \frac{Ni - H_0(h + x)}{h + x(1 + s)}$$

The energy input to the material is:

$$\int_D^{B_m} H_m(B_m^{'})dB_m^{'} = \frac{1}{2}B_m\left(H_m + \frac{M_0}{\mu_R}\right)$$

so net energy is added to the material. The magnetization work is:

$$\int_D^M \mu_0 H_m(M')dM' = \frac{1}{2}(M_0 + M)\left(H_m + \frac{M_0}{\mu_R}\right)$$

4.2.1 Hysteresis Loss

In starting at point A, traversing the hysteresis loop, and returning to the same point the energy input over one complete cycle is:

$$\int id\lambda = V\int \mu_0 H_m dM = V\int H_m dB_m = V4\mu_0 M_0 H_0 \tag{4.8}$$

and therefore this energy is lost as heat. Hysteresis power loss is therefore linearly proportional to the frequency at which the magnetic field changes direction.

4.3 Magnetization Force

As shown in Fig. 4.1, the magnetizable material is capable of being displaced in the x-direction in order to allow for examination of force on the material. The material is displaced a virtual distance dx in time dt. By the first law of thermodynamics, the input electrical energy $id\lambda$ plus input mechanical energy Fdx is equal to the increase in magnetic energy dW_m. Therefore, the electromagnetic force F_e is given by:

$$F_e = -i\frac{\partial\lambda(i,x)}{\partial x} + \frac{\partial W_m(i,x)}{\partial x} = -i\mu_0 NA\frac{\partial H_g(i,x)}{\partial x} + \frac{\partial W_m(i,x)}{\partial x} \tag{4.9}$$

Closed-form solutions for H_g and W_m were presented in the previous section. Because different expression for these quantities apply for each segment of the hysteresis loop, the complete expression for $W_m(i,x)$ is defined by several expressions, each applicable within certain ranges of H_m. The force can be in either direction if the hysteresis loop of the material has a nonzero area.

However, if the magnetization is zero and the relative permeability is greater than unity, the force can only be attractive.

4.4 Semi-Empirical Core Loss

The eddy-current losses analyzed in the previous chapter are greatly reduced by constructing the stator out of a stack of steel laminations. The core loss in steel laminations is empirically determined as a function of frequency and flux-density. This data is then fit by an analytic epxression. The core loss drag torque is:

$$T_{dr} = \frac{1}{\Omega} P_0 \left(\frac{p\Omega}{2\pi f_o} \right)^{\epsilon_F} \left(\frac{B}{B_o} \right)^{\epsilon_B} \tag{4.10}$$

where P_o, B_o, and f_o are the base power, flux density and frequency, respectively. ϵ_F and ϵ_B are the empirically-determined frequency and flux-density exponents, respectively. In the analysis in Chapter 7 the flux-density is constant. Therefore the symbol P_B is used to represent the core loss at constant flux-density, given by:

$$P_B \equiv P_0 \left(\frac{B}{B_o} \right)^{\epsilon_B} \tag{4.11}$$

Chapter 5

Stator Configuration

Stator designs are in general chosen in order to meet certain performance specifications. For aerial vehicle propeller motors zero torque ripple is not a performance specification. Stator winding configurations are in this chapter designed to maximize motor efficiency for given torque.

5.1 Design Comparisons

In the example motor design shown in Fig. 5.1, the tooth arclength in electrical radians is given by $\delta = \pi \frac{B_{ag}}{B_{sat}}$ where B_{ag} is the airgap flux-density and B_{sat} is the iron saturation flux-density. The teeth and yoke are of width $\delta R/p$, as shown in Fig. 5.1. The end-turn length is $4\pi/3$ times the average of the stator inner and outer radii as shown in the same figure.

As previously stated, the rotor can be either inside or outside of the stator. For a desired airgap flux-density, magnet thickness, and outer motor radius, the position of the rotor affects the airgap radius and the rotor-to-stator mass ratio. A large rotor-to-stator mass ratio produces high flux, requires large stator teeth and yields small winding area, whereas a small rotor-to-stator mass ratio yields the opposite. Which topology yields the highest torque is dependent on the motor parameters. The performance of the interior and exterior rotor layouts have been calculated for

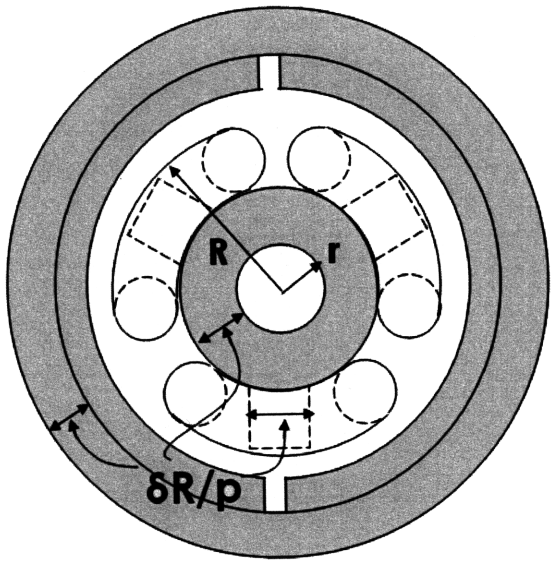

Figure 5.1: Exterior-rotor slotted-stator motor design

a fixed outer motor radius and motor mass. Fig. 5.2 shows which values of δ and rotor-to-stator radial height ratio yield equal performance for interior or exterior rotor layouts in this design study. The exterior rotor has higher torque for points below the line.

Another design choice is to remove the teeth and have the winding be located in the airgap. The suitable winding type also depends on δ and the rotor-to-stator radial height ratio. If the stator height is large compared to the rotor height and δ is small then the windings should be located in slots. If the converse is true and δ is sufficiently large, then airgap windings yield higher torque for given efficiency. For certain representative values of the motor parameters, the performance of slotted and airgap windings are equal along the δ vs. rotor-to-stator height ratio line shown in Fig. 5.2. The airgap winding yields higher torque for points above this line.

The exterior-rotor layout shown in Fig. 5.1 is chosen for the nano air-vehicle application because it maximizes motor performance based on the currently available permanent magnet and steel lamination materials. For modern permanent magnets, the optimal radial thickness of the rotor is much less than that of the stator. Therefore, motor performance is maximized by using an exterior rotor since this yields the largest airgap radius. High saturation-level steel is employed to

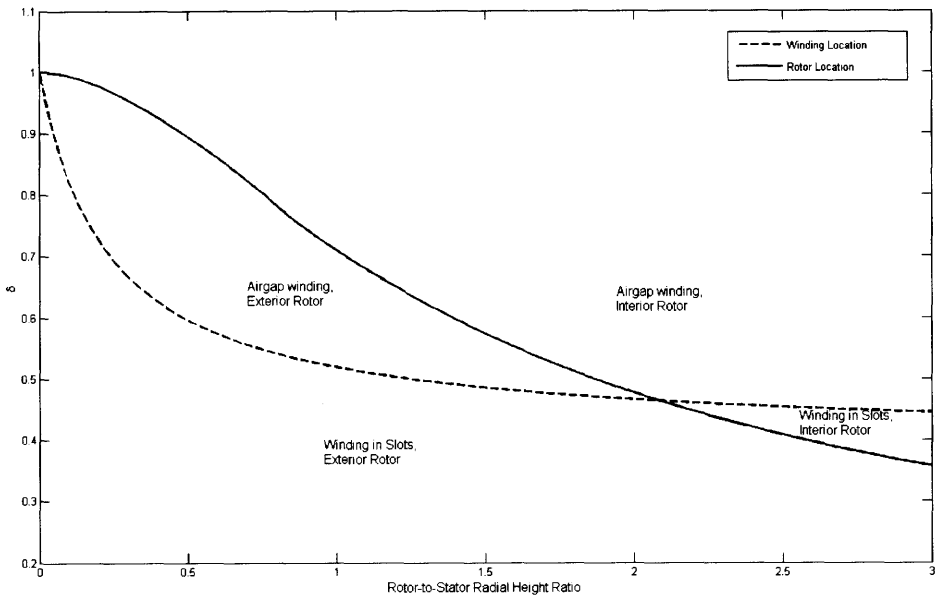

Figure 5.2: In this design study the inner rotor motor is optimal for points in the region above the solid line, and the outer rotor is optimal for the points below. Airgap windings are optimal for points above the dashed line, and windings in slots are optimal for points below it.

enable small tooth and yoke widths. This implies that the stator mass is best utilized by placing the windings in slots as opposed to in the airgap. When the external as opposed to internal rotor design is used the increased centrifugal forces remain acceptably small. An exterior rotor design also reduces the difficulty of affixing the magnets to the rotor.

Machine topologies other than those examined in this section have also been considered. As examined in [7], another possibility is to use a toroidal stator winding and employ both interior and exterior rotors. For a given motor mass, the performances of dual-rotor machines are comparable to those of optimized single-rotor machines.

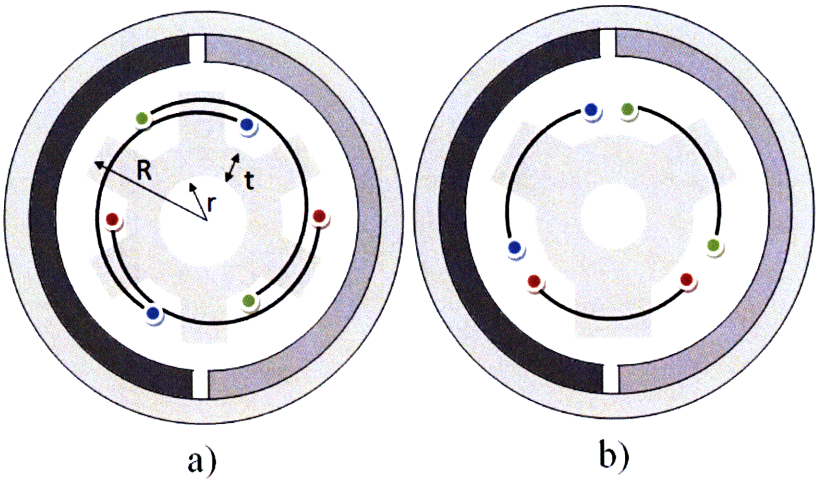

Figure 5.3: (a) Overlapping winding, (b) non-overlapping winding

5.2 Overlapping vs. Non-overlapping Winding

The winding of electrical wires in the stator slots is examined. Various ways of distributing the wires are possible depending on the number of slots in the stator and tradeoffs amongst these winding configurations are examined.

Winding wires in slots permits the use of a full-pitch winding since the wires may easily overlap, as shown in Fig. 5.3(a). An alternative shown in Fig. 5.3(b) is to reduce the resistance of the coil by shortening its span. In this diagram the fundamental pitch factor is reduced by a factor of $\sin(\pi/3) \approx .86$. The end-turn resistance is reduced by a factor of approximately $3/2$. The ratio of losses of these two windings is therefore given by:

$$\frac{P_{(o)}}{P_{(n)}} = \left(\frac{k_{w(n)}}{k_{w(o)}}\right)^2 \frac{4Lp/3 + 4\pi R/3}{2LQ/3 + 4\pi R/3} = \left(\frac{k_{w(n)}}{k_{w(o)}}\right)^2 \frac{p\frac{L}{R} + \pi}{p\frac{L}{R} + 2\pi/3} \tag{5.1}$$

where (n) denotes non-overlapping and (o) denotes overlapping. The highest-performance winding therefore depends on the motor dimensions and pole-number. However, in Section 7.2 it will be shown that, if the motor dimensions are unconstrained, the optimal value of $p\frac{L}{R}$ is a constant. Therefore, the losses ratio of optimized motor designs does not depend on the motor dimensions,

and the efficiency of non-overlapping and overlapping windings are comparable.

5.3 Fractional-Slot Winding

Small brushless motors are much easier to build using non-overlapping windings since they require fewer slots, only a fraction of a slot/pole/phase. For one rotor pole-pair there is only one possible winding configuration. However, for more than one pole-pair there is no longer a single possible winding configuration. This is because more than one multiple-of-three coil numbers exist, each of which are close in value to the pole number.

Torque is produced by the traveling wave of current in the coils of each phase interacting with the permanent magnet field. The wave of phase current has a lower fundamental spatial frequency than the field produced by the magnet poles, as shown in Fig. 5.4. Therefore, a certain harmonic of stator current interacts with the permanent magnet field. Knowing the value of this harmonic is important for analyzing a motor design, since if it is a multiple of three the motor will produce nearly no torque. The harmonic order can be determined by drawing the winding configuration as shown in Fig. 5.4. However, this is tedious and therefore this chapter develops a simple formula for the harmonic order as a function of the numbers of stator coils and rotor poles.

We begin by developing a systematic procedure for determing the locations and directions of the phase coils. When the permanent magnet array rotates, the phase of the flux-linkage is in general different for each coil and the phase between any two neighboring coils differs by a constant amount. Given that there are Q_s coils on the stator and p_r pole-pairs on the rotor, the phase difference between any two neighboring coils is

$$\angle\lambda = 2\pi\frac{p_r}{Q_s} \tag{5.2}$$

so the angle of the phasor of the n^{th} coil is $n\angle\lambda$. The number of coils Q_s must be an integer

multiple of 3. In general the coil phasors will not coincide with the phasors of the three-phase source. Each coil must be connected, in either the positive or negative direction, to the electrical phasor which is closest to its coil phasor. Grouping phasors by hand is time consuming so the Matlab function in Section B.2.1 generates a list of each coil's phase and direction.

Once the winding configuration is known, the harmonic can be determined as done for the examples in Fig. 5.4. The shaded rectangles represent the magnets and the coils. The symmetries shown by dashed lines define the North and South poles of the stator. Each symmetric North or South region of course consists of several coils having, in general, different senses. The poles must either all have the same polarity or there must be equal numbers of North and South poles to be symmetric, so if the number of poles is odd they share the same polarity. If the regions identified as the poles all have the same polarity then they must produce only even harmonics; if they alternate in polarity then they must produce only odd harmonics. In the 14 pole 18 slot design (c) there are two symmetric poles having opposite polarities, so $p_s = 1$ and the harmonics are odd. In the design with 9 slots and 6 poles, there are three poles having the same polarity. Some designs have ony one pole, as in (b). Design (d) has four alternating N-S poles. A design with 6 slots and 4 poles has $p_s = 1$, the two poles having the same polarity.

The current wave applied by the stator poles thus has either odd or even harmonics. For simplicity only the fundamental time harmonic of phase current is considered. The standing wave produced by each phase winding is the same as two traveling waves rotating in opposite directions. For harmonics which are multiples of three the sum of the waves from the three windings simplifies to zero. For other harmonic orders n the sum of traveling waves simplifies to [1]

$$F = \sum_n K_{wn} \frac{4}{n\pi} \frac{N_a I}{2p_s} \frac{3}{2} \cos(np_s\theta \pm p_r\Omega t) \tag{5.3}$$

$n = 1, -5, 7, -11, 13, -17...$ if stator poles are of same polarity

$n = 2, -4, 8, -10, 14, -16...$ if stator poles alternate in polarity

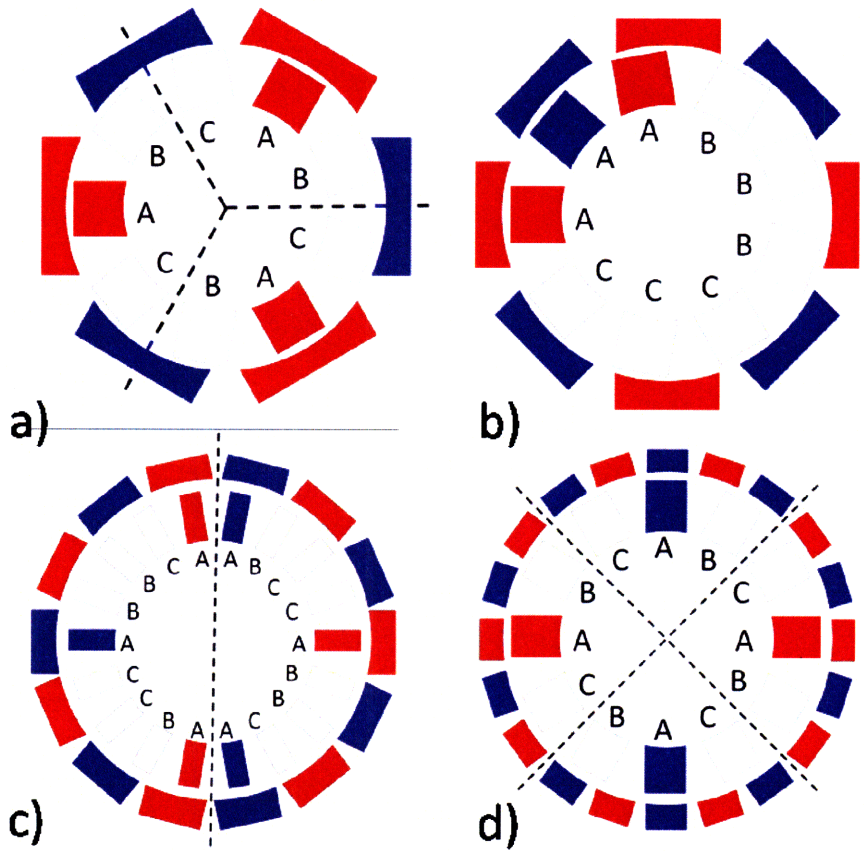

Figure 5.4: Outrunner motor coil and magnet layouts for determination of the number and polarity of stator poles. The inner shaded rectangles represent the coils of a single phase. a) $Q_s = 9, p_r = 3, p_s = 1.5$ same polarities b)$Q_s = 9, p_r = 4, p_s = .5$ c) $Q_s = 18, p_r = 7, p_s = 1$ alternating polarities, d) $Q_s = 12, p_r = 10, p_s = 2$ alternating polarities

and all other terms are zero. K_{wn} is the winding factor, N_a is the number of series turns per phase, and I is peak sinusoidal phase current. The $\pm$ sign in Eq. (5.3) must be chosen to make the harmonic wave that is traveling at the same speed as the rotor flux be forward rotating. If only the time fundamental is considered then this harmonic must have order $n_s = \frac{p_r}{p_s}$. If this is a multiple of three then no torque will be developed. Note that another reason why any design with an odd number of slots per phase can't have odd harmonics is because for symmetry there must be an integer number of wavelengths every 2π. Since the number of stator poles $2p_s$ for such a design must be odd, the harmonic orders n must all be even.

5.3.1 Formula for Higher Harmonic

In order to find a criterion for determining viable combinations of slots Q_s and poles $2p_r$, an obvious condition is $\frac{Q_s}{2p_r}$ not equal to 1, 1/2, 1/3... since for these a balanced three-phase winding is not achievable. Thus this condition requires that D not be a multple of three if D is defined as

$$m = \frac{Q_s}{6p_r} \Rightarrow \frac{T}{D} \tag{5.4}$$

where the fraction $\frac{T}{D}$ is reduced to lowest terms. This, in fact, holds in general even for non-unity T as may be verified. The necessary and sufficient condition for a balanced three-phase winding is:

$$D \neq 3n \tag{5.5}$$

where $n = 1, 2, 3....$ This requirement on slot-pole combinations has already been proposed in several publications.

For the example of D equal to three n_s is also a multiple of three since no torque is developed, and thus $D = n_s$ in that particular case. It may then be correctly suspected that n_s is always equal

to D. The higher harmonic n_s is therefore given by:

$$n_s = D = \frac{p_r}{p_s} \tag{5.6}$$

where D is the denominator of $\frac{Q_s}{2qp_r}$ when the fraction is reduced to lowest terms. It may be checked that D is an odd (even) number for designs producing odd (even) harmonics. This equation for p_s is useful because it eliminates the need for drawing the symmetry lines of the winding in order to determine the spatial harmonic content.

5.3.2 Winding Factors

The winding factor K_{wn} in Eq. (5.3) is the product of pitch and breadth factors. The pitch factor accounts for the fact that the EMFs induced in the coil-halves are not $180°$ out of phase. Since the harmonic orders are $\frac{n}{D}$, so that the first harmonic is synchronous with the rotor, the pitch factor is [1]

$$K_{pn} = \sin\left(\frac{n}{D}\frac{\alpha}{2}\right) \tag{5.7}$$

where the pitch is $\alpha = \pi\frac{2p_r}{Q_s}$ since each coil spans exactly one tooth. The breadth factor accounts for the fact that the EMF's induced in series-connected coils are not in phase. Notice that the number of unique phasors produced by Eq. (5.2) is $D\frac{Q_s}{2p_r} = \frac{Q_s}{2p_s}$, so the number of unique phasors per electrical phase is $\frac{Q_s}{6p_s} = Dm$. By adding together all of the coil phasors, the breadth factor may be derived as [1]

$$K_{bn} = \frac{\sin(\frac{n}{D}\frac{Dm\gamma}{2})}{Dm\sin(\frac{n}{D}\frac{\gamma}{2})} \tag{5.8}$$

where $\gamma = \frac{\pi}{3Dm}$ for any winding since the coils are modeled as being concentrated around each tooth.

5.4 Optimal Coil Number

By choosing the best coil number the motor torque is maximized. This is achieved by choosing a coil number which yields a low winding resistance and a high winding factor. The fundamental winding factor is maximized by selecting the coil number which is closest to the pole number. If there are multiple coil numbers with approximately the same winding factors, the smallest coil number is used since this yields the lowest winding resistance. For a certain number of rotor pole-pairs, two different fractional-slot winding configurations can have the same winding factor even if one winding has more axial conductors than the other.

For certain pole numbers the coil number one less than the pole number is possible. While this winding allows for balanced three-phase currents, the forces on the rotor are not balanced because the number of stator poles is unity. For example, this occurs for the motor having one rotor pole-pair, three stator coils, and therefore one stator pole.

Table (6.1) provides the coil number which maximizes torque for given efficiency and speed and which doesn't produce unbalanced radial forces. Notice that the coil number which maximizes torque for given terminal current magnitude is not the same as the coil number which maximizes torque for given efficiency and speed, because of the reduction in resistance provided by using a low coil number for a given pole number.

poles	4	6	8	10	12	14	16	18	20	22	24	26	28	30	32	34	36	38	40
coils	6	9	6	6	9	12	12	27	18	18	18	24	24	27	30	30	27	36	36

Table 5.1: Performance-optimizing coil number excluding those which produce unbalanced radial forces

Chapter 6

Empirical Data Reconciliation

In this chapter permanent magnet field distribution predictions are refined to correspond with empirical field distribution measurements. The predicted field distributions of motors similar to those shown in Fig. 6.1 are refined. The slots and slot-overhangs in these motors affect the field distribution as compared with the cylindrically symmetric smooth-stator model prediction. The source of differences between the empirical measurements and the three-dimensional field predictions are first understood. Factors are then determined to correct for effects not included in the simplistic model.

The permanent magnet field distribution in the winding region is the only quantity required to calculate output torque since the rotor is not salient. The open-circuit terminal voltage when the magnet array rotates is a function of the permanent magnet field distribution in the winding region and the winding configuration. In this chapter we solve for the applied field distribution as a function of the measured open-circuit voltage waveform and the measured motor dimensions, for either a conventional full-pitch concentrated winding or a fractional-slot winding. We then estimate the incremental permeability of the steel core as a function of the measured field distribution and the steel hysteresis loop. We measure the remanent flux density of the permanent magnets and predict the permanent magnet field distribution using the three-dimensional motor model.

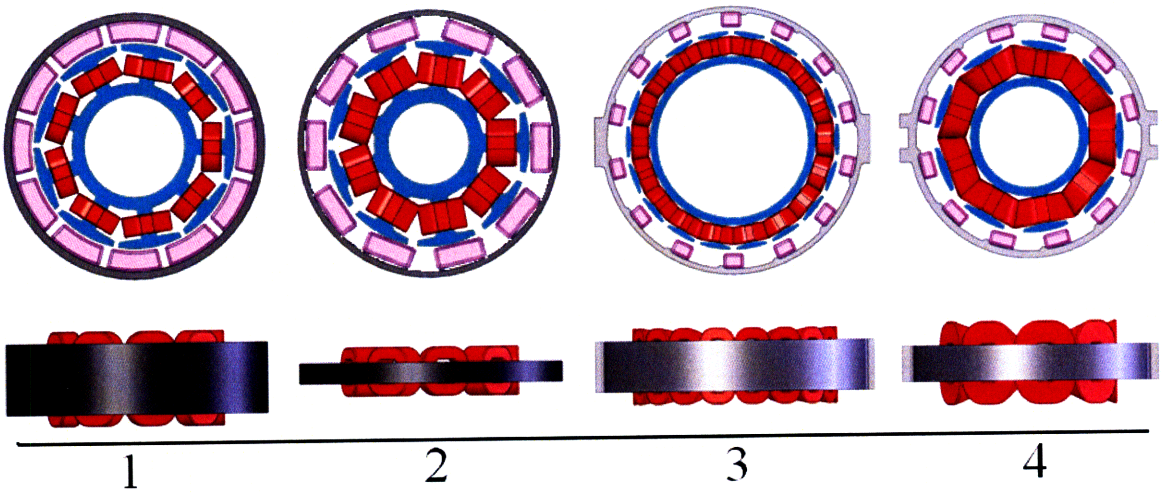

Figure 6.1: The four outrunner motors whose open-circuit terminal voltages were measured. Image courtesy of Don Fyler.

Motor	L	R	Q_s	p_r	$B_{re}[T]$	θ_m	tw	Steel	$p\lambda$	$R_a[\Omega]$
#1	3.1	5.0	9	6	1.27	$15\pi/16$	.6	unknown	.00355	3.4
#2	1.1	5.0	9	5	1.27	$2\pi/3$	.6	unknown	.00149	2.6
#3	2.6	5.3	18	7	1.04	$3\pi/8$	.3	Carpenter "49"	.00294	2.47
#4	1.9	4.9	9	6	1.05	$\pi/2$	.6	Carpenter "49"	.00269	3.33

Table 6.1: Measured motor dimensions. L=lamination stack length, R=stator airgap surface radius, B_{re}=remanent flux density measurement (courtesy of Don Fyler), θ_m=magnet arc in electrical radians, and tw is the width of each tooth. All dimensions are in mm. Relative motion gap=.2mm. End gap is assumed to be $g_z = 1mm$.

The empirical and modeled permanent magnet field distributions are found to differ. This is a mostly a result of the following two effects. Firstly, the stator slots increase the effective airgap compared to the smooth stator and also modulate the applied field distribution. Secondly, if the slot-overhangs are sufficiently thin they may become saturated while the tooth itself still operates in the high-permeability region. The impact of the saturated slot-overhangs makes it difficult to analyze these effects theoretically. The back EMF waveforms of the motors numbered $1-4$ in Fig. 6.1 have been measured in order to investigate these effects empirically.

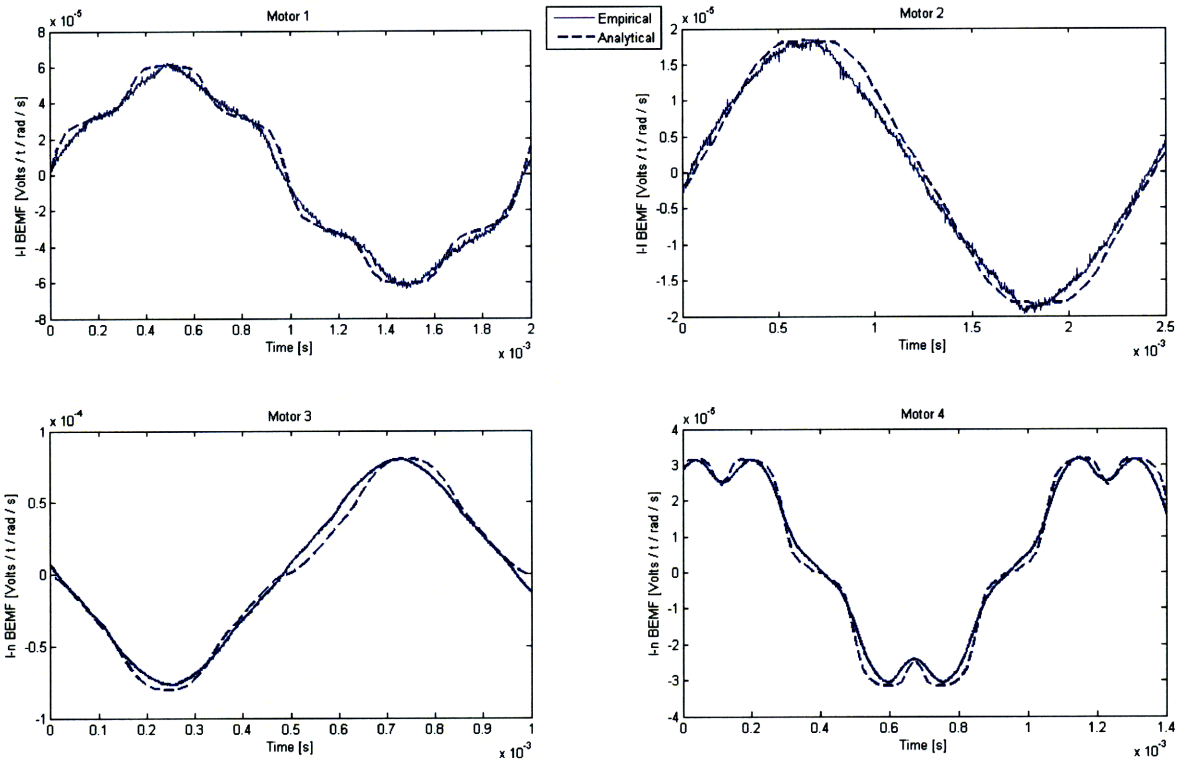

Figure 6.2: Measured and predicted fractional-slot back EMF waveforms [volts per rad/s per turn] of motors 1-4. Motors 1 and 2 are measured line-to-line whereas motors 3 and 4 are measured line-to-neutral.

6.1 Predicted Field Distributions

From the measured back voltage waveforms shown in Fig. 6.2 we determine the maximum internal flux assuming all flux flows through the teeth. The flux densities based on the tooth widths shown in Table 6.1 are calculated, and assuming motors 1 and 2 have the same laminations as 3 and 4, the data sheet indicates that the incremental permeability for all motors is approximately infinite.

The back EMF waveforms are calculated by the Matlab functions in Section B.2. As shown in Fig. 6.2, the shapes of the predicted and measured back EMF waveforms are in close agreement for motors 1,2, and 3. However, the measured waveform is found to be smaller by a constant empirical factor of $K_E = .84$, $K_E = .89$, $K_E = .79$ for motors 1,2, and 3 respectively. This is because the effective airgap is increased due to fringing fields in the slots. Since the shapes of the predicted and measured waveforms are in agreement, the slot-overhangs are assumed to not be saturated.

6.1.1 Slot-Overhang Saturation

The measured shape of motor 4's back EMF waveform is accurately predicted by the motor model if each tooth collects flux over an arclength of $2\pi/3$ instead of the full arclength of π used for motors 1-3. The empirical constant for this motor is found to be $K_E = .95$ because the stator polearc has been reduced. The decreased stator polearc indicates that the slot-overhangs may be saturated, and therefore the modulation of the measured field distribution by the slots is more pronounced. From Fig. 6.1 we notice that the slot overhangs in motors 3 and 4 are shallower than those of motors 1 and 2 which could contribute to their saturation. The measured back EMF of motor 3 does not indicate slot-overhang saturation because the magnet polearc is only $3\pi/8$ as compared to motor 4's magnet polearc of $\pi/2$ which creates higher flux in the same slot-overhang area.

6.2 Cogging Torque Data

Information about slot-overhang effects may be deduced from measurements of cogging torque as shown in this section. There are LCM(p,Q_s) cogging cycles per revolution each of which have identical torque profiles. The peak-to-peak cogging torque of Motor #1 was meassured to be $3.78e-5Nm$. The cogging torque of this motor is a maximum at $1/144$ of a revolution from the position shown in Fig. 6.1. From conservation of energy the change in magnetic energy when the rotor is displaced $1/144$ of a revolution is $dW_m = Td\theta = 1.89e-5 \cdot \frac{2\pi}{144} = 8.25e-7[J]$. The magnetic energy of the three magnet poles directly aligned with the teeth in Fig. 6.1 change the most over this rotation. This is because the magnets not aligned with teeth produce less cogging torque than those directly aligned with the teeth. The H field amplitude in a magnet becomes more negative by $dH = \sqrt{2dW_m/(3\mu_0)} = .66[A-m]$ when it is unaligned by $\pi/16$ electrical radians from a tooth. For future research, it would be productive to measure the cogging torque of a structure with equal numbers of magnets and teeth so that the effect of slotting can be better characterized.

6.3 Analytic Field Solution

In this section we find an analytic field solution which is equally as accurate as the more complicated Matlab model used to predict field distributions in the previous section. The motor model which is optimized in Chapter 7 permits the rotor and stator surfaces to be modeled as ferromagnetic boundaries. The essential magnetic behavior is described by the fundamental of the magnetic field. The fundamental radial flux density at the stator surface is:

$$\begin{aligned} B_r &= K_E B_{re} \frac{h_m}{g+h_m} \frac{k(R+g+h_m)/RK_p(kR)}{K_p(kR)I_p(k(R+g+h_m)) - I_p(kR)K_p(k(R+g+h_m))} \\ &\quad \times \left(\frac{I_p(kR)}{K_p(kR)} K_{p+1}(kR) - I_{p+1}(kR) \right) \end{aligned} \tag{6.1}$$

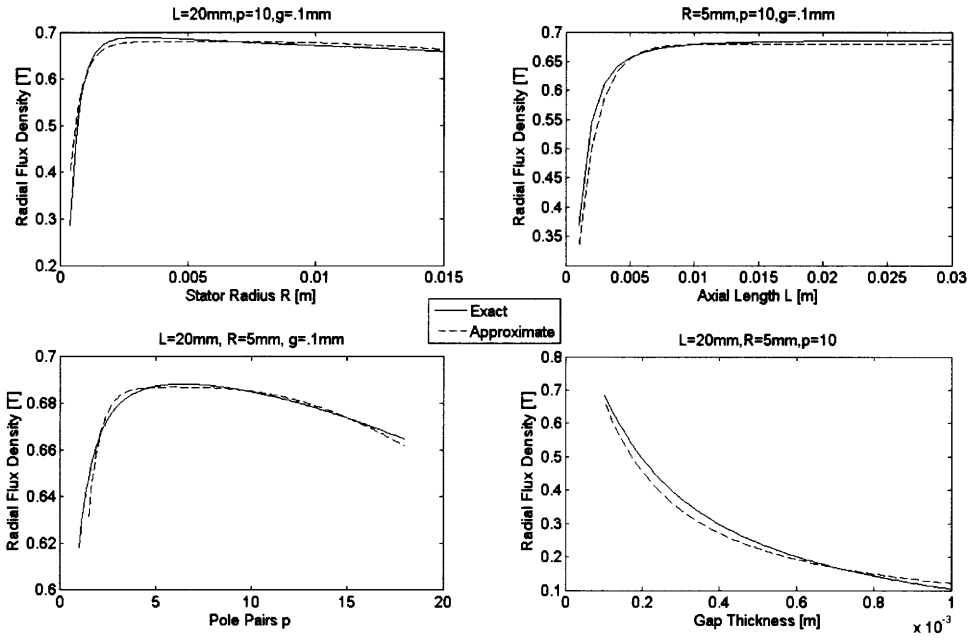

Figure 6.3: Exact dependence of radial flux-density on its parameters and approximate expressions fit to these curves

where $k = \pi/L$, L=axial length, R=stator surface airgap radius, g=gap thickness, p=number of pole-pairs, h_m=magnet radial height, and B_{re}=magnet remenant flux density.

6.3.1 Approximate Expression

In this subsection a simpler expression for Eq. (6.1) is found. This equation is plotted versus each of R,L,p, and g in Fig. 6.3, holding the other three parameters constant at the values given in the plot titles. The four separate dependencies of Eq. (6.1) on these four variables may each be modeled by fitting an approximate expression to the data. The approximate expressions, shown as dotted lines in the same plots, are in close agreement with the exact expression of Eq. (6.1) which

is based on empirical data. The approximate expressions are:

$$\begin{aligned}
B_r(R) &= K_E \frac{B_{re} h_m}{g + h_m} \left(1 - 9^{-1000R}\right) \left(1 - 16^{-\frac{.02}{R}}\right) \\
B_r(L) &= K_E \frac{B_{re} h_m}{g + h_m} \left(1 - 16^{-240L}\right) \\
B_r(p) &= K_E \frac{B_{re} h_m}{g + h_m} \left(1 - 16^{-.8p}\right) \left(1 - 9^{-\frac{27}{p}}\right) \\
B_r(g) &= K_E \frac{B_{re} h_m}{g + h_m} \left(1 - 9^{-\frac{.7e-4}{g}}\right)
\end{aligned}$$

An approximate expression is then determined as a function of all four variables. Three terms in the above approximate expressions have base 9 and the other three terms have base 16. Therefore, an approximation of Eq. (6.1) in terms of all four variables is deduced as:

$$B_{ag} = \frac{B_{re} h_m}{g + h_m} \left(1 - 9^{-k_{ml}\frac{R}{pg}}\right) \left(1 - 16^{-k_{al} p \frac{L}{R}}\right) \tag{6.2}$$

The constant $k_{ml} \approx .3$ is termed the magnet-leakage factor because it models the flux-shorting between magnets in the azimuthal direction. We define the constant $k_{al} \approx .5$ as the axial-leakage factor because it models the flux-shorting between magnets in the axial direction, an effect which is shown in Fig. 2.5. Increasing the radius for a given motor length and airgap decreases the amount of magnet-leakage because the magnet arclengths increase. However, increasing the radius also increases the relative amount of axial-leakage and therefore, as shown in Fig. 6.3(a), the flux-density versus R has a maximum. Increasing the pole number in a given radius increases the magnet-leakage but also decreases the end-leakage. As shown in Fig. 6.3(c), flux-density versus p therefore exhibits a maximum.

A simpler expression for airgap flux-density is finally derived. As the axial length L increases for a given airgap radius R, the amount of end-leakage decreases while there is no effect on the amount of azimuthal magnet-leakage. As p decreases the amount of azimuthal magnet-leakage decreases while there is very little effect on the amount of end-leakage. As airgap radius R increases

for a given L, the amount of end-leakage increases while the amount of azimuthal magnet-leakage simultaneously decreases. The net amount of leakage therefore varies little as R varies for a given L. Therefore, to good approximation the amount of leakage depends only on $\frac{L}{pg}$:

$$B_{ag} = \frac{B_{re}h_m}{g + h_m}\left(1 - e^{\frac{-L}{pg}}\right) \tag{6.3}$$

In the next chapter, the square of flux-density is given by the expression:

$$B_{ag}^2 = B^2\left(1 - e^{\frac{-L}{pg}}\right) \tag{6.4}$$

where $B = \frac{B_{re}h_m}{g+h_m}$. This has the same behavior as the more complicated expression but provides a necessary mathematical simplification.

Chapter 7

Motor Optimization

This chapter derives expressions for the optimal design parameters of the motor topology shown in Fig. 5.1. Analytic expressions for the optimal airgap radius and pole-number are first derived algebraically. The optimal stator inner radius is then investigated. An analytic expression is derived for the optimal pole-number as a function of steel lamination parameters. These symbolic parameters can characterize nearly any core material, and therefore this expression is not limited to the current state of material technology. The optimal rotor and stator design parameters are computed using the Monte Carlo method.

7.1 Performance Attribute

Motor efficiency for given torque and speed is:

$$\eta = \frac{P_{out}}{P_{in}} = \frac{T\Omega}{T\Omega + \frac{2}{3}\left(\frac{T}{p\lambda}\right)^2 R_a} \tag{7.1}$$

where λ is the phase flux-linkage and R_a is the phase winding resistance. Output torque for given efficiency and speed is:

$$T = \frac{1-\eta}{\eta}\Omega\frac{3}{2}\frac{(p\lambda)^2}{R_a} = \frac{1-\eta}{\eta}\Omega\frac{3}{2}(pB_{ag}2\pi RL)^2\frac{\sigma_c A_w}{L_w} \tag{7.2}$$

where B_{ag} is the airgap flux-density amplitude given by Eq. (6.2), σ_c is the conductivity of copper, A_w is the wire cross-sectional area, and L_w is the wire length. This expression is used as the performance attribute because of the mathematical simplification it provides.

7.2 Analytic Optimization

In this section the airgap radius R and rotor pole-number p are optimized by performing symbolic differentiation and algebraic manipulation. In particular, it is examined how differences in the way airgap flux-density is modeled affect the optimal values of R and p. Two models are analyzed which use different expressions for airgap flux-density. First, in Subsection 7.2.1, the airgap flux-density is approximated as being independent of R, L, and p. Second, in Subsection 7.2.2, the motor is more accurately modeled by employing the airgap flux-density expression which depends on R, L, and p. Apart from the differences in flux-density expressions, the two models are identical. The inner radius r and yoke thickness δ are zero in both of the models.

7.2.1 Constant Flux-Density Model

In this subsection the flux-density amplitude, B, is independent of R, L, and p and is given by $B = \frac{B_{re}h_m}{g+h_m}$. Torque is approximately proportional to:

$$T \propto (pBRL)^2\frac{\sigma_c R^2/p}{pL+R} \tag{7.3}$$

Torque divided by volume is proportional to:

$$\frac{T}{\pi R^2 L} \propto \frac{R^2 L}{L + R/p} \tag{7.4}$$

Torque at constant volume, as a function of R and p, is:

$$T \propto \left(pB\frac{V}{R}\right)^2 \frac{\sigma R^2/p}{p\frac{V}{R^2} + R} \tag{7.5}$$

The partial derivative with respect to R simplifies to:

$$\frac{\partial T}{\partial R} = \frac{pB^2V^2s}{\frac{pV}{R^2} + R}\left(\frac{2pV}{R^3} - 1\right) \tag{7.6}$$

and therefore R at maximum torque is:

$$R = (2pV)^{1/3} \tag{7.7}$$

and it is easily shown that p at maximum torque is infinite. This equation may be written as:

$$p\frac{L}{R} = \frac{1}{2} \tag{7.8}$$

Maximum torque is proportional to:

$$T \propto V^{3/2} \tag{7.9}$$

We see that in the limit $L \gg R$ torque density goes as R^2 which agrees with intuition because if only length is increased torque density becomes constant. Conversely, in the limit $R \gg L$ torque density goes as RL. Torque density has been shown to be maximized by the expression in Eq. (7.8). Therefore, torque density increases most by increasing radius only if $p\frac{L}{R} > \frac{1}{2}$. Otherwise, torque density increases most by increasing axial length.

Eq. (7.8) is proportional to the ratio of axial conductor length to end-turn length. The optimal motor dimensions may therefore be interpreted as occuring when each coil's ratio of axial length to radial arclength is $\frac{1}{2\pi}$. For a large pole-number, the wire resistance is dominated by axial length, and therefore increasing end-turn length by increasing radius creates a relatively small increase in resistance, and a net increase in torque density. For a given pole number, we see that an optimal stator aspect ratio exists even when the flux-density amplitude is approximated as being independent of the airgap dimensions.

In Subsection B.4.1, the Matlab symbolic manipulation toolbox is used to verify this analysis. In particular, the optimal pL/R ratio using this model is compared with the value of this ratio under the non-constant flux-density motor model which is discussed next.

7.2.2 Non-Constant Flux-Density Model

In this subsection, airgap flux-density is dependent on motor parameters through the expression in Eq. (6.4), whose form is discussed in Subsection 6.3.1. Torque is given by:

$$T \propto \left(1 - e^{-\frac{L}{pg}}\right)(pBRL)^2 \frac{R^2/p}{pL + R} \tag{7.10}$$

We maximize torque with respect to R and p while holding V constant, so torque is:

$$T \propto \left(1 - e^{-\frac{V}{\pi R^2 gp}}\right)\left(pB\frac{V}{\pi R}\right)^2 \frac{R^2/p}{p\frac{V}{\pi R^2} + R} \tag{7.11}$$

The partial derivatives of the above expression, when set equal to zero are easily shown to be:

$$\frac{\partial T}{\partial R} = -e^{\frac{-L}{pg}}\frac{2L}{g} - \left(1 - e^{\frac{-L}{pg}}\right)\frac{pR}{pL + R}\left(1 - 2p\frac{L}{R}\right) = 0 \tag{7.12}$$

$$\frac{\partial T}{\partial p} = -e^{\frac{-L}{pg}}\frac{1}{pg} + \left(1 - e^{\frac{-L}{pg}}\right)\left(\frac{1}{L} - \frac{p}{pL + R}\right) = 0 \tag{7.13}$$

where the expression for V has been substituted back in. Eq. (7.12) divided by Eq. (7.13) is seen to be:

$$2Lp = -Lp\left(1 - 2p\frac{L}{R}\right) \tag{7.14}$$

$$\Rightarrow p\frac{L}{R} = \frac{3}{2} \tag{7.15}$$

Eq. (7.12) is then:

$$-e^{\frac{-L}{pg}}\frac{1}{pg} + \left(1 - e^{\frac{-L}{pg}}\right)\left(\frac{1}{L} - \frac{2pg}{5R}\right) = 0 \tag{7.16}$$

which has the solution given by:

$$\begin{aligned} R &= \frac{10^{1/5}3^{4/5}}{12}\left(-\sqrt{5} - 1 + i\sqrt{2}\sqrt{5 - \sqrt{5}}\right)\frac{\left[-V^2g^4\pi^3(5W(-1, -.4e^{-.4}) + 2)\right]^{1/5}}{\pi g W(-1, -.4e^{-.4}) + 2} \\ &\propto g^{-1/5}V^{2/5} \end{aligned} \tag{7.17}$$

This expression for R is purely real, as is shown by the script in Section B.4.1. The complex function $W(K, X)$ is given by the Matlab function `lambertw`. The optimal pole-number is then given by:

$$p = \frac{3\pi}{2}\frac{R^3}{V} \propto g^{-3/5}V^{1/5} \tag{7.18}$$

and axial length is proportional to:

$$L = \frac{V}{\pi R^2} \propto g^{2/5}V^{1/5} \tag{7.19}$$

The optimal values of p and R are seen to depend on g because, intuitively, the optimal p and R decrease as the amount of magnet-leakage, which is proportional to g, increases. R and L can therefore no longer depend on volume to the $1/3$ power based on consideration of their dimensions. However, the ratio pL/R still does not depend on V or g, because p and L depend on volume to a power which is half the power to which R depends on V.

The result that pL/R does not depend on V or g is non-obvious, as it could equal V/g^3 for example. Given that pL/R is constant and that p and L depend on V to the same power, dimensional analysis yields two equations in two unknowns which are easily solved for the powers to which R, L and p depend on V. Their dependence on g then follows from consideration of dimensions. The Matlab script in Section B.4.1 verifies these results by performing algebraic manipulation.

7.2.3 Comparison

Including the dependence of airgap flux-density on R, L, and p has been seen to affect the optimization results in two ways. First, it has given the pole-number a finite optimal value, which has been seen to increase with stator volume. Second, it has changed the optimal pL/R ratio. Under the constant flux-density model, the quantity pL/R is a constant whose value is equal to $1/2$. Under the non-constant flux-density model, the result that pL/R is independent of V and g cannot be seen based on dimensional analysis alone, but has to be seen through Eq. (7.15).

The optimal value of this quantity increases to $3/2$ when the complete expression for flux-density is used. This is because the optimal design wants to reduce both the flux-leakage as well as end-turn resistance, and therefore uses a larger length and smaller radius. We notice that in the flux-leakage factor the base may have any value, not just e, in order to yield this analytic result for pL/R.

7.3 Stator Inner Radius

This section considers the selection of an inner radius, r. In the previous section, the airgap radius R was found to be limited by the resistance of the end-windings for a given number of pole-pairs. By increasing the number of pole-pairs, the outer radius and the torque density could be increased. However, the pole number was found to be limited by the leakage effects. As a result, optimal values for the pole number and outer radius were determined.

However, a larger torque density could be achieved if it were possible for a given mass to increase the airgap radius without also decreasing the airgap flux-density. Increasing the pole-number beyond its optimal value determined in the previous section would increase the optimal airgap radius, but this would decrease flux-density so much that torque would decrease. An increase in outer radius can be achieved, without requiring an increase in pole-number or decrease in flux-density, by building the stator in an annular, as opposed to solid, form. By increasing the inner radius, outer radius, and axial length together, neither the stator mass, L-to-R ratio, or the airgap flux-density change, but the torque increases. Another advantage of this annular shape is that it accomodates a structural tube which is useful for mounting the motor to the vehicle.

However, building the stator in an annular shape increases the fraction of stator mass consisting of the yoke. The annular shape allows R to be larger, for a given stator mass, than for a solid-shaped stator. However, for a given total stator mass and number of poles, this requires the yoke and teeth to carry more flux which therefore increases their size and consequently the iron-to-copper mass ratio. As we increase r, the dimension $R - r$ eventually decreases until it equals $\delta R/p$, at which point the copper mass is zero and no torque is produced. Therefore, there exists an optimal value of r which depends on the tooth-arc δ. The larger δ, the smaller the inner radius at which the torque is maximized.

Therefore, it is important to consider δ in the motor model when we attempt to optimize the inner radius. Here, the winding area is:

$$A_w = \pi R^2 - \pi(r + \delta R/p)^2 - 2p(R - r - \delta R/p)\delta R/p \tag{7.20}$$

This expression is valid if the rectangular teeth intersect with the yoke before the teeth intersect with each other. This is the case if:

$$2\pi\left(r + \delta\frac{R}{p}\right) > Q_s\left(\delta\frac{R}{p}\right) \tag{7.21}$$

where Q_s is the number of coils. The densities of copper and iron are assumed to be equal, and the winding space factor is assumed to be unity, so that the stator mass is proportional to:

$$V = \pi(R^2 - r^2)L \tag{7.22}$$

We wish to perform optimization with respect to all three variables r, R, and p in terms of the known parameters V and δ. The analytic technique used in the previous section does not yield closed-form solutions due to the increased complexity of the model. In this section, we begin by finding an approximate analytic expression for the optimal R value as a function of given values of p, V, and δ. We then calculate the optimal r as a function of pole-number p. Optimization of the pole-number is the subject of Section 7.6.

We first seek an approximate expression for the optimal R value in terms of p, V, and r. It will later be verified that the expression derived for r equal to zero, $\frac{pL}{R} = \frac{3}{2}$, also holds when r is nonzero. With the stator volume as given above, the solution for R is:

$$R = \frac{\left[12\gamma^2(9pV + \sqrt{(9pV)^2 - 12\gamma^2 r^6})\right]^{2/3} + 12\gamma^2 r^2}{6\gamma\left[12\gamma^2(9pV + \sqrt{(9pV)^2 - 12\gamma^2 r^6})\right]^{1/3}} \tag{7.23}$$

where $\gamma = \frac{1.5 \cdot 20}{\pi}$.

In solving for the optimal inner radius, care must be taken because multiple local maxima and minima may exist. The script in Section B.4.2 performs the optimization by symbolically differentiating torque with respect to r, and then numerically solving for r as a function of V, p, and δ. The optimal r is shown in Fig. 7.1 versus each of these variables separately.

As shown in this figure, the optimal inner radius goes as δ to the power $-.5$. Because V is the only dimensional quantity which the approximate optimal value of r depends upon, r increases with V to the $1/3$ power as shown in Fig. 7.1. In this figure it is also found that r increases as p to

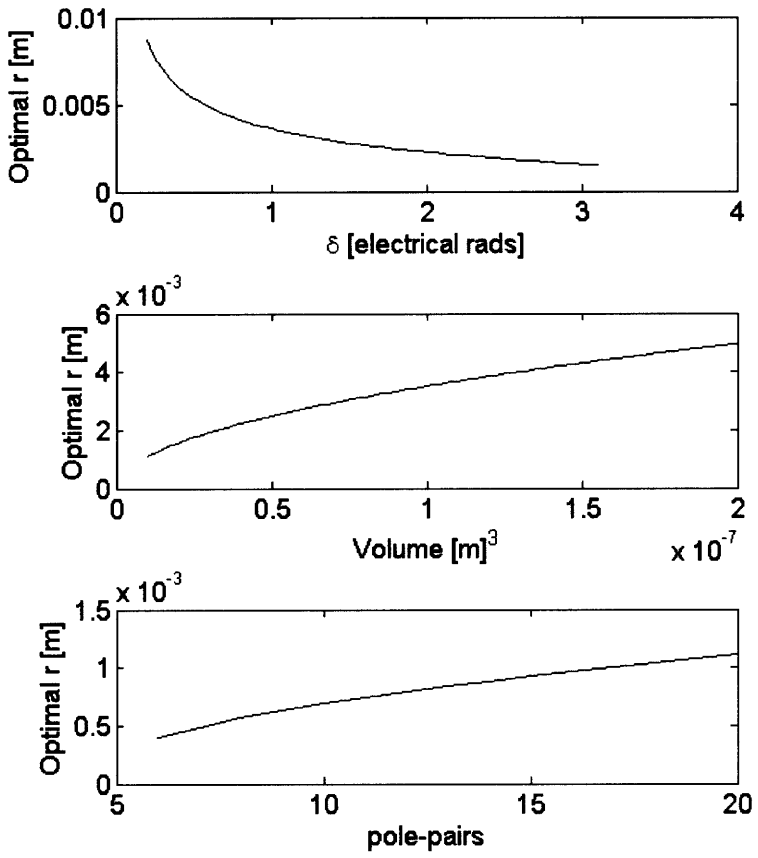

Figure 7.1: The optimal amount of inner radius increase as it depends on the tooth-arc δ, the stator volume, and the number of pole-pairs.

the approximately .7 power. The optimal amount of inner radius increase is given by:

$$r \propto V^{1/3} p^{.7} \delta^{-.5} \tag{7.24}$$

This equation is verified using Monte Carlo optimization in the next section.

7.4 Monte Carlo Method

This section uses the Monte Carlo method to compute optimal design parameters for given numerical values of material parameters. In the previous two sections optimal design parameters have been studied by assuming that δ and V are constants. To be sure, however, δ is not a constant since it depends on p, R, and magnet height h_m, all of which we seek to optimize. Precise design optimization must therefore use both remanent flux-density B_{re} and saturation flux-density B_{sat} as known constants instead of δ, but this increases the number of constant material parameters. The derivative of torque with respect to h_m in terms of all the constant parameters is not tractable.

In this chapter the optimal designs are determined by computing torque for random combinations of design parameters. Each design parameter is given a foating-point value randomly selected from a predefined interval. For each random motor design, efficiency and motor active mass are calculated. Random designs are solved until it is deemed that the optimal designs are known with a high enough certainty.

Monte Carlo optimization is implemented in the script in Section B.4.3. Motor efficiency, η, is calculated by:

$$\eta = \frac{T_d \Omega_d}{T_d \Omega_d + T_d^2 / T} \tag{7.25}$$

where T_d and Ω_d are the required output torque and speed, respectively, and T is the torque at 50% efficiency and speed $\Omega = 1$ [rad/s]. Motor active mass is given in grams by:

$$m = \pi L((R + h_m + \delta R/p)^2 - r^2) \cdot 7.5 \cdot 10^6 \tag{7.26}$$

Torque is calculated using the expression for winding area given in Eq. (7.20) and the script verifies that the inequality in Eq. (7.21) is satisfied for each design variation.

The optimized design parameters and predicted efficiency are shown in Fig. 7.2 as a function of active mass. As shown in this script, the results are presented for $T_d = .001[N - m]$, $\Omega_d =$

$1000[rad/s]$, $k_{ml} = .3$, $B_{re} = 1T$, $B_{sat} = 2T$, $g = .2mm$. At this same torque and speed, the measured efficiencies of prototype motors #1-#4 are: $\eta = .76, .46, .73, .68$, respectively. The active masses of these motors are $m = 2.19, .95, 1.45, 1.16$ grams, respectively.

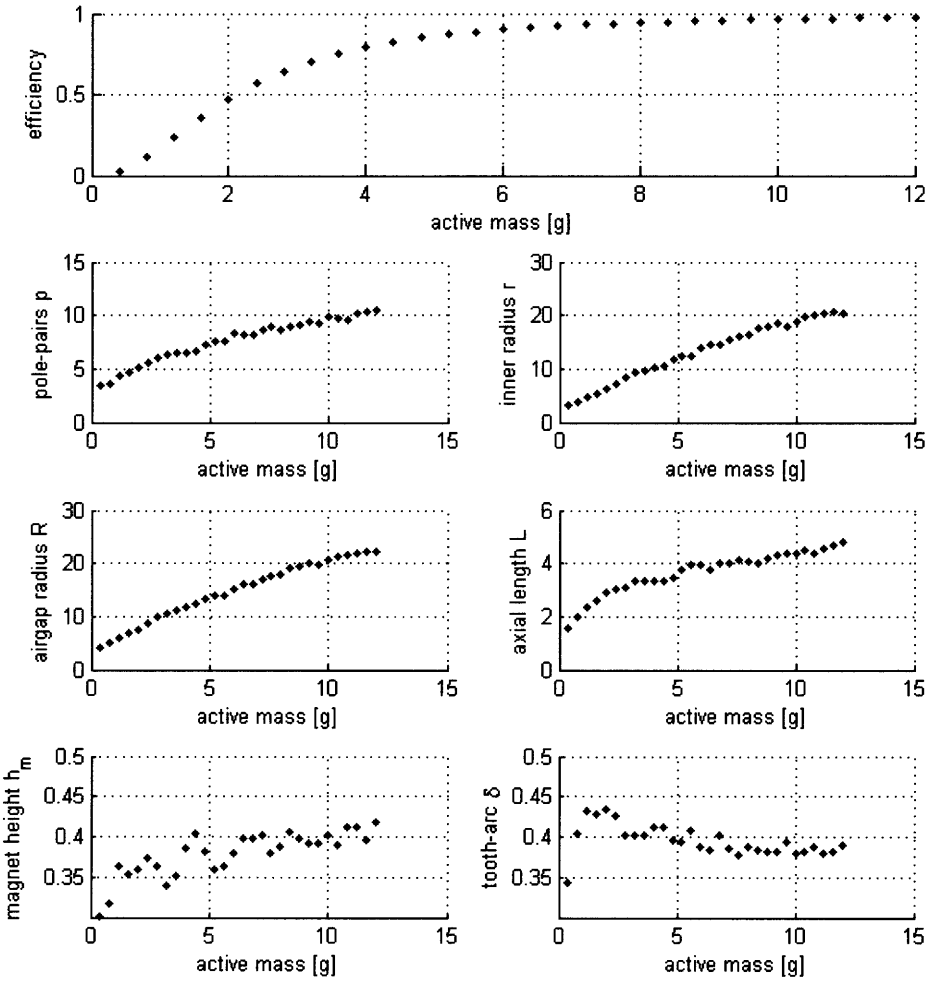

Figure 7.2: Optimal design parameters versus motor active mass, calculated by the script in Section B.4.3. All dimensions are given in millimeters (mm). The tooth-arc is in electrical radians.

7.5 Comparison of Results

In this section the Monte Carlo optimization results are compared with the analytic expressions derived in Subsections 7.2.1, 7.2.2 and 7.3. Heuristic curve fits of the results shown in Fig. 7.2 are provided in Table. 7.1. The expression given for efficiency is valid only for efficiencies $\eta < 20\%$. As shown in Fig. 7.2, the initial slope of the efficiency vs. mass curve is zero, and efficiency increases faster than linear with mass in the very low efficiency regime.

$$\eta = 1 - 12^{-.15m}$$

$$p = 5.1m^{.304} \qquad r = 6.0m^{.52}$$

$$R = 6.9m^{.491} \qquad L = .85m^{.416}$$

$$h_m = .54m^{.142} \qquad \delta = 1.14m^{-.03}$$

Table 7.1: Heuristic curve fits of the curves in Fig. 7.2

The Monte Carlo analysis predicts that the airgap radius increases as motor mass to the .49 power. The expression derived using the non-constant flux-density model, Eq. (7.17), predicts an increase with mass to the .4 power. The expression derived for a given pole-number, Eq. (7.7), predicts an increase to the $1/3$ power. The Monte Carlo results show that pole number increases as motor mass to the approximately .30 power. The non-constant flux-density model, Eq. (7.18), predicts an increase with mass to the .2 power. Eq. (7.23) was derived based on the assumption that Eq. (7.8) was valid, while strictly speaking it only applies when the inner radius is zero. The Monte Carlo results verifies this assumption that Eq. (7.8) holds approximately, though not exactly, when the inner radius is nonzero.

The model presented in Section 7.3, from which Eq. (7.24) was derived, does apply when the inner radius is nonzero. Since the Monte Carlo results have shown that $V \propto m$, Eq. (7.24) becomes:

$$r \propto m^{1/3} p^{.7} \delta^{-.5}$$

$$m^{.52} \stackrel{?}{=} m^{1/3} m^{.21} m^{-.01} = m^{.53}$$

The Monte Carlo optimization results are therefore approximately consistent with Eq. (7.24).

7.5.1 Constrained Optimization

The pole-number may need to be constrained to a value other than the optimal value suggested by the Monte Carlo results. Eq. (7.24) gives the optimal r value when p is constrained to a certain value for a certain motor mass. The optimal value of R given constrained values of p and r is given approximately by Eq. (7.23). By employing the Monte Carlo results a much simpler expression for the optimal R is given by:

$$R \propto m^{1/3} p^{1/3} r^{\epsilon_r} \tag{7.27}$$

The Monte Carlo results provide the information that $m^{.491} \propto m^{1/3} m^{.1} m^{.52x}$. We then solve for the result that $\epsilon_r = .12$.

This equation and Eq. (7.24) provide the optimal dependence of R and r on motor mass when the number of poles is constrained.

7.6 Core Loss Consideration

In this section the dependence of the optimal pole-number on steel parameters is investigated. Steel core losses increase with electrical frequency, and the impact of this on the optimal pole-number has thus far been neglected. An analytic expression for the optimal pole-number is found as a function of the optimal p vs. m data computed in the previous section, as well as the symbolic iron parameters B_{sat}, P_B, and ϵ_f.

7.6.1 Output Torque Expression

We begin by deriving an expression for output torque (no drag loss) as a function of p, for constant values of motor mass m and iron saturation level B_{sat}. To this end we first find for which pole-number output torque has its maximum. We then find an analytic expression for output torque versus pole-number which has this as its peak value.

The optimal pole-number and corresponding maximum output torque versus motor mass m is given in the prevous section. To find how the torque-vs.-mass and pole-number-vs.-mass relationships depend on the material parameter B_{sat}, the script in Section B.4.3 is run for several values of B_{sat}. The output torque T and maximum pole-number for any given value of mass increases with B_{sat}, given approximately by:

$$T \approx 2000 m^{1.3} B_{sat}^{.9} \equiv C_T m^{\epsilon_1} B_{sat}^{\epsilon_2} \tag{7.28}$$

$$p \approx .5 m^{.3} B_{sat}^{.33} \equiv C_p m^{\epsilon_3} B_{sat}^{\epsilon_4} \tag{7.29}$$

where symbolic variables are defined for the constants derived from the Monte Carlo results.

We now find output torque as a function of pole-number. This is modeled by an equation of the form:

$$T = a_1 p - b_1 p^3 \tag{7.30}$$

The value of p at the maximum of this, $p = \sqrt{\frac{a_1}{2b_1}}$, is set equal to Eq. (7.29). Eq. (7.29) is plugged into Eq. (7.30) and set equal to Eq. (7.28). These two equations are solved for the values of a_1 and b_1:

$$\begin{aligned} a_1 &= \frac{3C_T}{2C_p} m^{\epsilon_1 - \epsilon_3} B_{sat}^{\epsilon_2 - \epsilon_4} \\ b_1 &= \frac{C_T}{2C_p{}^3} m^{\epsilon_1 - 3\epsilon_3} B_{sat}^{\epsilon_2 - 3\epsilon_4} \end{aligned}$$

7.6.2 Optimal Pole Number

We now find the pole-number at the maximum of shaft torque. Using Eq. (7.30), shaft torque at 50% efficiency is given by:

$$T = \Omega(a_1 p - b_1 p^3) - \frac{1}{\Omega} P_B \left(\frac{p\Omega}{2\pi f_o} \right)^{\epsilon_F} \frac{\delta}{\pi} m \tag{7.31}$$

The optimal torque may be solved in a closed form if $\epsilon_F = 1.5$. Then the derivative of Eq. (7.31) with respect to p is

$$\begin{aligned} \frac{dT}{dp} &= \Omega \frac{1-\eta}{\eta}(a_1 - 3b_1 p^2) - \frac{1}{\Omega} P_B \left(\frac{\Omega}{2\pi f_o} \right)^{1.5} \frac{\delta V}{\pi} 1.5\sqrt{p} && (7.32) \\ &\equiv a_2 - b_2 p^2 - c_2 \sqrt{p} && (7.33) \end{aligned}$$

where we have defined variables for the coefficeints of p. The zeros of this equation can be found in a closed form. The optimal number of poles is given by:

$$p = \frac{3^(1/3)}{24} (2^{1/3}\gamma + 2^{1/12})^2 \left(82^{1/6} 3^{1/3} \frac{\gamma a_2 b_2 - 12 c_2 \beta}{b_2 \beta \gamma} - \sqrt{2}\gamma\beta^2 \right) \tag{7.34}$$

where

$$\beta = \left(9b_2c_2^2 + b_2\sqrt{3(256a_2^3b_2 + 27c_2^4)}\right)^{1/3}$$

$$\gamma = \sqrt{\frac{\beta^2 - 42(2/3)3(1/3)a_2b_2}{b_2\beta}}$$

Fig. 7.3 plots the optimal pole-number expression versus P_B for $B_{sat} = 1T$ and $B_{sat} = 2T$ and constant values for the other motor parameters. The optimal pole number decreases as the core loss increases for constant iron flux density. For motors of volume one cm^3 and of airgap flux density .8 Tesla, the nickel-iron steel alloy Carpenter "49" in .006" thick laminations provides a good tradeoff between saturation flux-density and core loss. The empirical core loss of this alloy at 400 Hz and $B_{sat}1.4[T]$ is $P_B = 2mW/lb$.

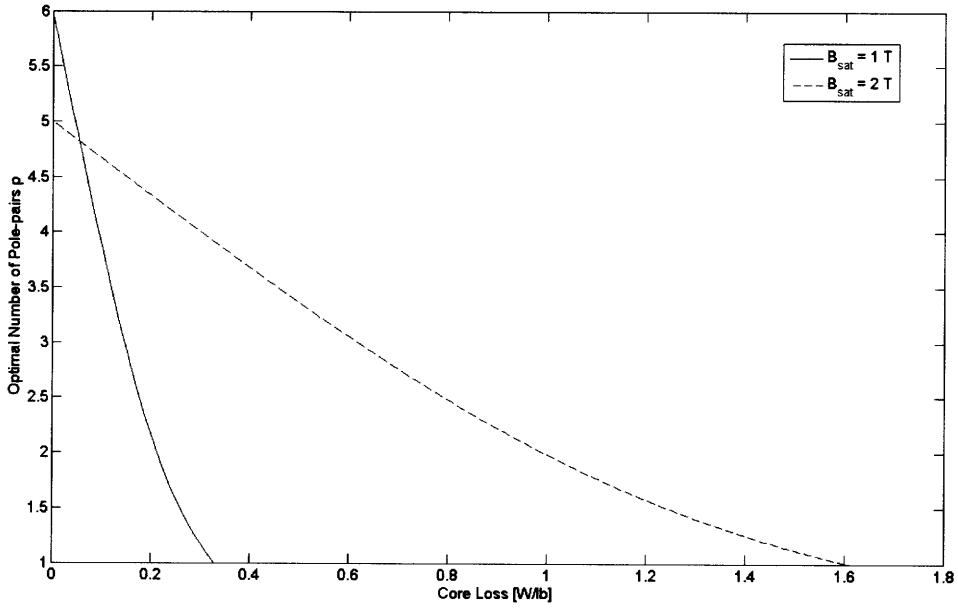

Figure 7.3: Optimal pole-number vs. core loss for two values of B_{sat}

Chapter 8

Conclusion

This thesis peforms a design study of radial-flux permanent magnet machines in order to characterize their performance versus motor mass. A three-dimensional magneto-static model has been developed, and an analytic expression for airgap flux-density has been derived which corresponds well with empirical measurements. The Monte Carlo method has been used to compute optimal values for all of the design parameters as a function of mass for given material parameter values, and these results have been compared with analyically-derived optimal relationships.

The motor model developed in this thesis is consistent with the measured performance characteristics of the prototype motors presented in Chapter 6. However, none of the proposed optimal designs shown in Table 7.1 have been empirically characterized. Quantatative values for the empirical factor K_E and magnet leakage factors k_{ml} and k_{al} are most accurately determined from empirical measurements. Because optimal designs have not been built, the predicted optimal efficiency and design parameters may differ from empirical results. Indeed, the usefulness of the results summarized in Table 7.1 lies in that these results give the analytic forms of, but not necessarily the quantatative data for, formulas for assisting with the rapid design of slotted radial-flux machines over a wide range of machine mass.

8.1 Further Investigation Possibilities

Further research can look into optimizing the slot-overhang design. While the effects of slot-overhang saturation on the field distribution have been analyzed using empirical data, optimization of the slot-overhang design has not been performed. The slot-overhang arclength and radial height, which affect the magnet-leakage and cogging torque ripple, could be the focus of future optimization. After fabricating stators with different slot-overhang arclengths, cogging torque measurements could be used to calculate the magnet-leakage factors and compare the performances of the designs. Whereas precise optimization of the pole-number, for example, does not dramatically increase motor performance, the size of the slot-overhangs does significantly affect the amount of magnet-leakage. In connection with the optimization of slot-overhang arclength, better methods for containing the conductors within the slots may need to be developed. Current winding methods require large overhangs in order to retain the conductors.

If it is possible to expand the scope of the research, the lift provided by the propeller should be characterized. In this thesis motor torque has been optimized assuming the motor's diameter is unconstrained, and the optimal designs are found to have smaller length-to-diameter ratios than those of currently available motors. However, for given propeller size the lift decreases as the motor diameter increases. By characterizing the propeller efficiency as a function of motor diameter and speed, the motor speed and size may be more accuately optimized.

Appendix A

Finding Torque Capability

This derivation is from Beaty and Kirtley [1]. The first step is to convert the three-phase stationary quantities into two-phase stationary quantities and the zero-sequence quantity. The stationary quantities are then mapped to the rotating d-q frame quantities by the rotation matrix and the zero-sequence quantity is left unchanged. The currents, fluxes, and voltages are written in the form:

$$\underline{I}_{dq} = \begin{bmatrix} i_d \\ i_q \\ i_0 \end{bmatrix}, \underline{I}_{ph} = \begin{bmatrix} i_a \\ i_b \\ i_c \end{bmatrix}$$

The normalized mapping is easily seen to be:

$$\underline{I}_{dq} = \underbrace{\frac{2}{3} \begin{bmatrix} \cos\theta & \sin\theta & 0 \\ -\sin\theta & \cos\theta & 0 \\ 0 & 0 & 1 \end{bmatrix} \begin{bmatrix} 1 & -\frac{1}{2} & -\frac{1}{2} \\ 0 & \frac{\sqrt{3}}{2} & -\frac{\sqrt{3}}{2} \\ \frac{1}{2} & \frac{1}{2} & \frac{1}{2} \end{bmatrix}}_{\underline{\underline{T}}} \underline{I}_{ph}$$

where $\underline{\underline{T}}$ denotes Park's Transformation which simplifies to:

$$\underline{\underline{T}} = \frac{2}{3}\begin{bmatrix} \cos\theta & \cos(\theta - \frac{2\pi}{3}) & \cos(\theta + \frac{2\pi}{3}) \\ -\sin\theta & -\sin(\theta - \frac{2\pi}{3}) & -\sin(\theta + \frac{2\pi}{3}) \\ \frac{1}{2} & \frac{1}{2} & \frac{1}{2} \end{bmatrix}$$

The open-circuit armature voltages are:

$$\underline{V}_{ph} = \frac{d}{dt}\underline{\lambda}_{ph}$$

The voltages in the d-q frame are:

$$\begin{aligned} \underline{V}_{dq} &= \underline{\underline{T}}\underline{V}_{ph} = \underline{\underline{T}}\frac{d}{dt}\underline{\lambda}_{ph} \\ &= \underline{\underline{T}}\frac{d}{dt}(\underline{\underline{T}}^{-1}\underline{\lambda}_{dq}) \\ &= \frac{d}{dt}\underline{\lambda}_{dq} + \underbrace{(\underline{\underline{T}}\frac{d}{dt}\underline{\underline{T}}^{-1})}_{*}\underline{\lambda}_{dq} \end{aligned}$$

where the matrix denoted by * simplifies to:

$$* = \begin{bmatrix} 0 & -\frac{d\theta}{dt} & 0 \\ \frac{d\theta}{dt} & 0 & 0 \\ 0 & 0 & 0 \end{bmatrix}$$

The d-q frame voltages are therefore:

$$V_d = \frac{d\lambda_d}{dt} - \omega\lambda_q$$

$$V_q = \frac{d\lambda_q}{dt} + \omega\lambda_d$$

where $\omega = \frac{d\theta}{dt}$.

Instantaneous armature power is:

$$P = V_a I_a + V_b I_b + V_c I_c$$

This maps to:

$$P = \frac{3}{2} V_d I_d + \frac{3}{2} V_q I_q + 3 V_0 I_0$$

or

$$P = \omega \frac{3}{2} (\lambda_d I_q - \lambda_q I_d) + \frac{3}{2} \left(\frac{d\lambda_d}{dt} I_d + \frac{d\lambda_q}{dt} I_q \right) + 3 \frac{d\lambda_0}{dt} I_0$$

Recalling that $\omega = p\Omega$ and $P = T\Omega$ output torque is:

$$T = \frac{3}{2} p (\lambda_d i_q - \lambda_q i_d)$$

The permanent magnet field produces flux λ_f on the d-axis. Since the d-q fluxes are:

$$\begin{aligned} \lambda_d &= L_d I_d + \lambda_f \\ \lambda_q &= L_q I_q \end{aligned}$$

torque is given by:

$$T = \frac{3}{2} p (\lambda_f + (L_d - L_q) I_d) I_q$$

When $L_d = L_q$ the optimal control of current is:

$$\underline{I}_{dq} = \begin{bmatrix} 0 \\ I \\ 0 \end{bmatrix}$$

If $\theta = \omega t - \pi/2$ then the optimal phase currents form a balanced set:

$$\underline{I}_{ph} = T^{-1}\underline{I}_{dq} = \begin{bmatrix} I\cos\omega t \\ I\cos(\omega t - \frac{2\pi}{3}) \\ I\cos(\omega t + \frac{2\pi}{3}) \end{bmatrix}$$

Appendix B

MATLAB Code

B.1 3D Field Solution

B.1.1 fieldsolver

```
% This function solves for field distributions by computing the
% field amplitude for each magnetization harmonic


% Inputs
% p = rotor pole-pairs
% Ri = stator hollow radius
% ts = stator yoke radial height
% hs = slot height
% ag = airgap thickness
% hm = magnet radial height
% tr = rotor backiron radial height
% thetam = magnet pole-arc
% delt = stator tooth-arc
% L = axial length
% Brem = magnet remanent flux density
```

```
% gz = axial gap

% Outputs
% Btot = radial flux density at stator surface. 2D array

function Btot = fieldsolver(p, Ri, ts, hs, ag, hm, tr, thetam,
 delt, L, Brem, gz)

global p u1 u2 u3 u4 u5 u6 u7 R1 R2 R3 R4 R5 R6 delt Ms ps ks

R1 = Ri;
R2 = R1 + ts;
R3 = R2 + hs;
R4 = R3 + ag;
R5 = R4 + hm;
R6 = R5 + tr;

thetaz = pi/(1 + 2*gz/L);
k = thetaz/L;
u0 = 4*pi*1e-7;
u1 = u0;
u4 = u0;
u5 = u0;
u7 = u0;

% solve for iron permeabilities
ps = p; % pole pairs for calculating permeability
ks = k; % axial wavenumber for calculating permeability
Ms = Brem/u0*thetam/pi; % amplitude for calculating permeability
u2 = fzero('nonlinear', u0*[1 5e10]);
u3 = u2;
```

```
u6 = u2;


do = pi/50/p;
dz = Lm/50;
dA = R3*do*dz;
theta = 0:do:(2*pi-do)/p;
z = -Lm/2-gz:dz:Lm/2+gz;

Btot = 0;
for m = 1:2:100/p
    for n = 1:2:21
        pm = m*p;
        kn = n*k;
        Mn = Brem/u0*16/(pi^2*m*n)*sin(m*thetam/2)*sin(n*thetaz/2);
        Br3 = bcs(pm,kn,Mn);
        Btot = Btot + Br3*cos(kn*z)'*cos(pm*theta);
    end
end

Btot = repmat(Btot,1,p);
```

B.1.2 bcs

```
% This function computes the field amplitudes
% for sinusoidal magnetization

% Inputs
% pm = azimuthal harmonic wavenumber
% kn = axial harmonic wavenumber
% Mn = mangetization harmonic amplitude
```

```
% Outputs
% Br3 = radial flux density amplitude at stator airgap radius

function Br3 = bcs(pm,kn,Mn)
global u0 u1 u2 u3 u4 u5 u6 u7 R1 R2 R3 R4 R5 R6

% solve particular solution in magnet region
rv = R4:(R5-R4)/100:R5;
X0 = [0; 0];
[r,X] = ode45('partic', rv, X0);
sip4 = X(1,1);
dsip4 = (X(2,1)-sip4)/(r(2)-r(1));
Xl = length(X);
sip5 = X(Xl,1);
dsip5 = (sip5-X(Xl-1,1))/(r(Xl)-r(Xl-1));

I1 = besseli(pm,kn*R1);
K1 = besselk(pm,kn*R1);
I2 = besseli(pm,kn*R2);
K2 = besselk(pm,kn*R2);
I3 = besseli(pm,kn*R3);
K3 = besselk(pm,kn*R3);
I4 = besseli(pm,kn*R4);
K4 = besselk(pm,kn*R4);
I5 = besseli(pm,kn*R5);
K5 = besselk(pm,kn*R5);
I6 = besseli(pm,kn*R6);
K6 = besselk(pm,kn*R6);

dI1 = I1*pm/R1 - kn*besseli(pm+1,kn*R1);
dI2 = I2*pm/R2 - kn*besseli(pm+1,kn*R2);
```

```
dI3 = I3*pm/R3 - kn*besseli(pm+1,kn*R3);
dI4 = I4*pm/R4 - kn*besseli(pm+1,kn*R4);
dI5 = I5*pm/R5 - kn*besseli(pm+1,kn*R5);
dI6 = I6*pm/R6 - kn*besseli(pm+1,kn*R6);
dK1 = K1*pm/R1 - kn*besselk(pm+1,kn*R1);
dK2 = K2*pm/R2 - kn*besselk(pm+1,kn*R2);
dK3 = K3*pm/R3 - kn*besselk(pm+1,kn*R3);
dK4 = K4*pm/R4 - kn*besselk(pm+1,kn*R4);
dK5 = K5*pm/R5 - kn*besselk(pm+1,kn*R5);
dK6 = K6*pm/R6 - kn*besselk(pm+1,kn*R6);

mat = [
u1*dI1 -u2*dI1 -u2*dK1 0       0       0       0       0       0       0       0       0;
0      u2*dI2  u2*dK2  -u3*dI2 -u3*dK2 0       0       0       0       0       0       0;
0      0       0       u3*dI3  u3*dK3  -u4*dI3 -u4*dK3 0       0       0       0       0;
0      0       0       0       0       u4*dI4  u4*dK4  -u5*dI4 -u5*dK4 0       0       0;
0      0       0       0       0       0       0       u5*dI5  u5*dK5  -u6*dI5 -u6*dK5 0;
0      0       0       0       0       0       0       0       0       u6*dI6  u6*dK6  -u7*dK6;
I1 -I1 -K1 0   0   0   0   0   0   0   0   0;
0  I2  K2  -I2 -K2 0   0   0   0   0   0   0;
0  0   0   I3  K3  -I3 -K3 0   0   0   0   0;
0  0   0   0   0   I4  K4  -I4 -K4 0   0   0;
0  0   0   0   0   0   0   I5  K5  -I5 -K5 0;
0  0   0   0   0   0   0   0   0   I6  K6  -K6;
];

src = [
    0 0 0 ...
    -u0*Mn + u5*dsip4...
    -(-u0*Mn + u5*dsip5)...
    0 0 0 0 ...
    sip4...
    -sip5...
    0]';
```

```
C = linsolve(mat, src);


A3 = C(4);
B3 = C(5);
A4 = C(6);
B4 = C(7);
Br3 = u3*(A3*dI3 + B3*dK3);
```

B.1.3 partic

```
% This function is used to numerically solve the
% inhomogeneous modified bessel equation


function der = partic(r,X)
global pm kn Mn
dR1dt = X(2);
dR2dt = -1/r*X(2) + (kn^2 + pm^2/r^2)*X(1) + 1/r*Mn;
der = [dR1dt; dR2dt];
end
```

B.1.4 nonlinear

```
% This function describes a representative B-H curve of
% steel in the first and third quadrants


% Inputs
% x = current guess of permeability


% Outputs
% F = difference between flux-density calculated from field model
%     and calculated from B-H curve
```

```
function F = nonlinear(x)
global Ms ps ks

u2=x
Br3 = bcs(ps,ks,Ms);

Hr3 = abs(Br3)/u2;
SBr3 = log(1000*Hr3)/10;
F = Br3-SBr3;
```

B.2 Back EMF Calculation

B.2.1 winding

```
% This function generates the fractional-slot winding configuration
% by rounding each back EMF phasor to the closest electrical phasor

% Inputs
% q = number of phases (2 or 3)
% p = number of rotor poles

% Outputs
% coils = list of each coil's phase and sense,
          designated by posiive/negative integers

function coils = winding(q,p)
Qsv = [3 6 9 6 6 9 12 12 27 18 18 18 24 24 27 30 30 27 36 36];
Qs = Qsv(p);

m = zeros(2*q, 2);
```

```
for n = 1:1:q
    m(2*n-1,:) = [n n];
    x = n + q/2;
    if x >= q+1
        x = x-q;
    end
    m(2*n,:) = [x -n];
end
sm = sortrows(m);
seq = sm(:,2);

coils = zeros(1,Qs);
for i = 1:Qs
    fr = rem(i*p,Qs)/Qs;
    coils(i) = seq(floor(2*q*fr)+1);
end
```

B.2.2 bemfsolver

```
% This function solves for the back EMF waveforms

% Inputs
% Btot = radial flux density at stator surface. 2D array
% p = rotor pole-pairs
% q = number of phases
% do = theta increment used to compute Btot
% dz = z increment used to compute Btot
% R3 = stator airgap radius

% Outputs
% emf = backemf waveforms for all q phases
```

```
function emf = bemfsolver(Btot, p, q, do, dz, R3)

% convert the fractional-slot coils list to q-by-Qs matrix of +/- 1's
% alternatively, coils and Qs can be made to
% represent conventional winding
coils = winding(q,p);
Qs=length(coils);
cm = zeros(q,Qs);
for i = 1:1:Qs
    c = coils(i);
    cm(abs(c),i) = sign(c);
end

% calculate the flux linkages
[nr nc] = size(Btot);
de = nc/Qs;
ee = [];
for be = 1:1:nc-1;
    Bs = [Btot(:,be:nc) Btot(:,1:be-1)];
    fv = [];
    for st = 1:de:nc-de+1
        fv = [fv sum(sum(Bs(:,st:st+de-1)))];
    end
    ee = [ee cm*fv'];
end

% calculate the back EMF
emf = diff(ee,1,2)*R3*dz;
% plot(emf')
```

B.3 Eddy Current Solution

B.3.1 Model Parameters Values

```
% params
% This file defines the input parameters

u0 = 4*pi*1e-7;
p = 7;
m = p-1;
n = -p-1;

sigma = 8.4e7; % rod conductivity
u = 2000*u0;  % rod permeability

Brem = 1.4; % remanent flux density
M = Brem/u0;
tang = pi/2; % magnet polearc
ur = u0; % recoil permeability

ag = .1e-3; % airgap thickness
hm = 1e-3; % magnet radial height
R = 5e-3; % rod radius
Ri = R + ag;
Ro = Ri + hm;

dr = R3/1000;  % differential radius
rvec = [1e-7:dr:R3]; % radius vector
do = .01; % differential angle
theta = 0:do:2*pi; % angle vector

RPMv = 1:100:1.2e4; % speed vector
```

```
ommv = pi/30*RPMv;
omm = 2*pi*1e3/60;
```

B.3.2 Airgap Field Distribution

```
% This script calculates the airgap field distribution
% in Sec. 3.1.2

params % get model parameter values

Btot = 0;
p0 = p;
for nn = 1:2:21;
    p = p0*nn;
    m = p-1;
    n = -p-1;
    om = p*omm;
    M = Brem/u0*4/(nn*pi)*sin(nn*tang/2)

    alp = (1-j)/sqrt(2/(om*u*sigma));
    Hr = -j*p/(alp^2*R)*besselj(p,alp*R);
    Ho = 1/alp/2*(besselj(p-1,alp*R) - besselj(p+1,alp*R));

    mat = [
    Ro^p        Ro^-p       0            0             0;
    -ur*p*Ri^m  ur*p*Ri^n   u0*p*Ri^m    -u0*p*Ri^n    0;
    -Ri^p       -Ri^-p      Ri^p         Ri^-p         0;
    0           0           u0*p*R^m    -u0*p*R^n     -u*Hr;
    0           0           j*p/R*R^p    j*p/R*R^-p    -Ho;
    ];

    src = [-Ro*M/(1-p^2) -Brem+Brem/(1-p^2) M*Ri/(1-p^2)  0   0]';
```

```
    C = linsolve(mat,src);
    A2 = C(3);
    B2 = C(4);
    Br = u0*p*(A2*R^m - B2*R^n);

    Bnn = real(Br*exp(j*(-p*theta)));
    Btot = Btot + Bnn;
end
plot(theta,Btot)
```

B.3.3 Drag Loss

```
% This script calculates the drag torque using each of the
% two methods presented in Sec. 3.1.3 and plots them

params % get model parameter values

Fo = [];
Pd = [];
for omm = ommv
    om = p*omm;
    alp = (1-j)/sqrt(2/(om*u*sigma));
    Hr = -j*p/(alp^2*R)*besselj(p,alp*R);
    Ho = 1/alp/2*(besselj(p-1,alp*R) - besselj(p+1,alp*R));

    mat = [
    Ro^p          Ro^-p         0             0              0;
    -ur*p*Ri^m    ur*p*Ri^n     u0*p*Ri^m     -u0*p*Ri^n     0;
    -Ri^p         -Ri^-p        Ri^p          Ri^-p          0;
    0             0             u0*p*R^m      -u0*p*R^n      -u*Hr;
    0             0             j*p/R*R^p     j*p/R*R^-p     -Ho;
```

```
    ];

    src = [-Ro*M/(1-p^2) -Brem+Brem/(1-p^2) M*Ri/(1-p^2)  0   0]';

    C = linsolve(mat,src);
    AC = C(5);
    Jz = AC*besselj(p,alp*rvec);
    Pdi = [Pd 1/4*2*pi*sum(rvec.*abs(Jz).^2)/sigma*dr];

    Br = -AC*u4*j*p./(alp^2*rvec).*besselj(p,alp*rvec);
    FLD = real(Jz.*conj(Br));
    FL = 2*pi/4*sum(rvec.*FLD)*dr;
    Fo = [Fo FL];
end
Tpow = Pd./ommv;
Tlor = Fo*R;

plot(RPMv,Tpow)
hold on
plot(RPMv,Tlor,'r')
```

B.4 Optimization

B.4.1 Analytic Method

```
% In this script two motor models are solved analytically.
% The optimal pL/R ratios are calculated for two models:
% the first does not contain the leakage factor, the second
% does, and the two are otherwise identical. When the leakage
% factor is included, the optimal pL/R ratio is calculated
% in this script to be three times that without leakage.
```

```
% The solution for R in the leakage model is shown to be
% purely real.

% Constant Flux-Density Model (Sec. 7.2.1)
clear all;
syms V R L p g B s  % variables (s=sigma)

% Optimization w.r.t. R; V held constant

L = V/(pi*R^2);
T = (p*B*R*L)^2*(s*R^2/p)/(p*L+R);
Rdot = diff(T,'R');
S = solve(Rdot,'R');
R = S(2);          % positive solution for R
L = V/(pi*R^2);
p*L/R              % ans = 1/2

% Non-constant Flux-Density Model (Sec. 7.2.2)
clear all;
syms V R L p g B s

% Optimization w.r.t. p and R; V held constant

L = V/(pi*R^2);
T = (1-exp(-L/(p*g)))*(p*B*R*L)^2*(s*R^2/p)/(p*L+R);
pdot = diff(T,'p');
Rdot = diff(T,'R');
S = solve(pdot,Rdot,'p','R');
p = S.p(4);
R = S.R(4);
L = V/(pi*R^2);
```

```
p*L/R              % ans = 3/2

V = 1e-7;
p = 4;
g = 2e-4;
subs(S.R)
subs(R)            % purely real solution
```

B.4.2 Optimal Inner Radius

```
% This script numerically solves the zeros of the
% analytical torque derivative with respect to r
% as a function of V, p, and delta.

% (a) maximum r versus delta

clear all;
rv = [];
dv = .2:.05:pi;
for d = dv
  r = fzero(@(x) vsd(x,d),.01);
  rv = [rv r];
end
subplot 311
plot(dv,rv)
hold on
xlabel('\delta [electrical rads]')
ylabel('Optimal Inner Radius r')

% (b) maximum r versus volume

rv = [];
```

```
dv = 1e-8*(5:.2:20);
for V = dv
  r = fzero(@(x) vsV(x,V),0.01);
  rv = [rv r];
end
subplot 312
plot(dv,rv,'-')
xlabel('Volume [m]^3')
ylabel('Optimal Inner Radius r')
hold on

% (c) maximum r versus pole number

rv = [];
dv = 5:1:15;
for p = dv
  r = fzero(@(x) vsp(x,p),.001);
  rv = [rv r];
end
subplot 313
plot(dv,rv)
xlabel('pole-pairs')
ylabel('Optimal Inner Radius r')

% Compute symbolic derivative expressions
% These results are inserted into the functions which
% fzero solves.

clear all;
syms r p
d=pi/3;
```

```
V = 1e-8;
n=1.5;
a = ((108*V*p+12*(-12*r^6*pi^2*n^2+81*V^2*p^2)^(1/2))*pi^2*n^2)^(1/3);
R = 1/6/pi/n*a + 2*r^2*pi*n/a;
L = V/(pi*(R^2-r^2));
T = (p*R*L)^2*(pi-d)*((R^2-(r+d*R/p)^2)/p)/(p*L+R);
dr = diff(T,'r')     % =x in vsp(r,p)

clear all;
syms r d
p=10;
V = 1e-8;
n=1.5;
a = ((108*V*p+12*(-12*r^6*pi^2*n^2+81*V^2*p^2)^(1/2))*pi^2*n^2)^(1/3);
R = 1/6/pi/n*a + 2*r^2*pi*n/a;
L = V/(pi*(R^2-r^2));
T = (p*R*L)^2*(pi-d)*((R^2-(r+d*R/p)^2)/p)/(p*L+R);
dr = diff(T,'r')     % =x in vsd(r,d)

clear all;
syms r V
d=pi/3;
p = 10;
n=1.5;
a = ((108*V*p+12*(-12*r^6*pi^2*n^2+81*V^2*p^2)^(1/2))*pi^2*n^2)^(1/3);
R = 1/6/pi/n*a + 2*r^2*pi*n/a;
L = V/(pi*(R^2-r^2));
T = (p*R*L)^2*(pi-d)*((R^2-(r+d*R/p)^2)/p)/(p*L+R);
dr = diff(T,'r')     % =x in vsV(r,V)
```

B.4.3 Monte Carlo Method

```
% This script implements Monte Carlo motor optimization
% as discussed in Sec.7.6.

% model parameters

ag = 2e-4; % airgap thickness
Bsat = 2;  % iron saturation level
Bre = 1;   % remanent flux density
km = .3;   % magnet leakage factor
Om = 1000; % desired speed
Td = .001; % desired torque

dm = .4;  %mass increment
opd = zeros(5000/dm,8); %array of parameters

for n = 1:1:1e8
    v = [2 24]*1e-3;
    r = v(1) + (v(2)-v(1))*rand(1);

    v = [4 25]*1e-3;
    R = v(1) + (v(2)-v(1))*rand(1);

    v = [.1 10]*1e-3;
    L = v(1) + (v(2)-v(1))*rand(1);

    v = [5 30];
    p = v(1) + (v(2)-v(1))*rand(1);

    v = [.1 2]*1e-3;
    hm = v(1) + (v(2)-v(1))*rand(1);
```

```
    Bag = Bre*hm/(ag+hm)*(1-exp(-1/ag*km*L/p));
    d = pi*Bag/Bsat;      %delta
    tw = d*R/p;    %tooth and yoke thickness

    Aw = pi*R^2 - pi*(r+tw)^2 - 2*p*tw*(R-(r+tw));
    T = (p*Bag*2*pi*R*L)^2 *sig*Aw/p/(L*p+R);
    mass = pi*((R + hm + tw)^2 - r^2)*L * 7.5e6; %motor active mass [grams]

    %update array with highest performance design
    in = floor(mass/dm)+1;
    if T > opd(in,2)
        opd(in,:) = [in*dm T p r R L hm d];
    end
end

% plot results

opd = opd(1:80,1:8);
figure(1)
m = opd(:,1);
Tv = opd(:,2);
etac = Td*Om./(Td*Om + Td^2./Tv);
subplot(4,2,1:2)
scatter(m,etac,'k.')
xlabel('active mass [g]')
ylabel('efficiency')
grid on

subplot(4,2,3)
scatter(m,opd(:,3),'k.');
```

```
xlabel('active mass [g]')
ylabel('pole-pairs p')
grid on

subplot(4,2,4)
scatter(m,1e3*opd(:,4),'k.');
xlabel('active mass [g]')
ylabel('inner radius r')
grid on

subplot(4,2,5)
scatter(m,1e3*opd(:,5),'k.');
xlabel('active mass [g]')
ylabel('airgap radius R')
grid on

subplot(4,2,6)
scatter(m,1e3*opd(:,6),'k.');
xlabel('active mass [g]')
ylabel('axial length L')
grid on

subplot(4,2,7)
scatter(m,1e3*opd(:,7),'k.');
xlabel('active mass [g]')
ylabel('magnet height h_m')
grid on

subplot(4,2,8)
scatter(m,opd(:,8),'k.');
xlabel('active mass [g]')
```

```
ylabel('tooth-arc \delta')
grid on
```

Bibliography

[1] H. Beaty and J. L. Kirtley. *Electric Motor Handbook.* McGraw-Hill, New York, 1998.

[2] N. Bianchi and S. Bolognani. Fractional-slot pm motors for electric power steering systems. *Int. J. Vehicle Autonomous Systems*, 2(3/4):189–200, 2004.

[3] P. Campbell. Comments on 'energy stored in permanent magnets'. *IEEE Transactions on Magnetics*, 36(1):401–403, 2000.

[4] R. Deodhar. Prediction of cogging torque using the flux-mmf diagram technique. *IEEE Transactions on Industry Applications*, 32(3):569–576, 1996.

[5] D. Hanselman. *Brushless Permanent-Magnet Motor Design.* McGraw-Hill, New York, 1994.

[6] J. Ofori-Tenkorang. *Permanent-Magnet Synchronous Motors and Associated Power Electronics for Direct-Drive Vehicle Propulsion.* PhD thesis, Massachusetts Institute of Technology, 1996.

[7] R. Qu, M. Aydin, and T. Lipo. Performance comparison of dual-rotor radial-flux and axial-flux permanent-magnet bldc machines. In *Electric Machines and Drives Conference*, volume 3, pages 1948–1954, 2003.

[8] M. Rahman. Ipm motor drives for hybrid electric vehicles. *Motor Drives*, 2(3/4):189–200, 2007.

[9] F. Reif. *Fundamentals of Statistical and Thermal Physics*. McGraw Hill, New York, 1965.

[10] P. Salimen. *Fractional Slot Permanent Magnet Synchronous Motors for Low Speed Applications*. PhD thesis, Lappeenranta University of Technology, 2004.

[11] M. Zahn. *Electromagnetic Field Theory*. McGraw-Hill, New York, 1994.

[12] M. Zahn. Power dissipation and magnetic forces on maglev rebars. *IEEE Transactions on Magnetics*, 33(1):1022–1030, 1997.